Metal Polluted White Dwarfs with 21 μm IR excesses from JWST/MIRI: Planets or Dust?

John H. Debes [1,2] Sabrina Poulsen [3] Ashley Messier [4] Susan E. Mullally [1] Katherine Thibault [5,6]
Loïc Albert [5,6] Misty Cracraft [1] Érika Le Bourdais [5] Patrick Dufour [5] Tom Barclay [7,8]
J. J. Hermes [9] Mukremin Kilic [3] David Lafrenière [10,11] Fergal Mullally [12] William Reach [13] AND
Elisa Quintana [7]

[1] The Space Telescope Science Institute
3700 San Martin Dr.
Baltimore, MD 21218, USA
[2] Aura, for ESA
[3] Homer L. Dodge Department of Physics and Astronomy, University of Oklahoma, 440 W. Brooks St., Norman, OK, 73019 USA
[4] Five College Astronomy Department, Amherst College, Amherst, MA 01002, USA
[5] Département de physique and Institut Trottier de recherche sur les exoplanètes, Université de Montréal, C.P. 6128, Succ. Centre-ville,
Montréal, H3C 3J7, Québec, Canada
[6] Observatoire du Mont-Mégantic, Université de Montréal, C.P. 6128, Succ. Centre-ville, Montréal, H3C 3J7, Québec, Canada
[7] NASA Goddard Space Flight Center, Greenbelt, MD 20771, USA
[8] University of Maryland, Baltimore County, Baltimore, MD 21250, USA
[9] Department of Astronomy, Boston University, 725 Commonwealth Avenue, Boston, MA 02215, USA
[10] Institut Trottier de Recherche sur les exoplanètes, Université de Montréal, C.P. 6128, Succ. Centre-ville, Montréal, H3C 3J7, Québec,
Canada
[11] Département de Physique, Université de Montréal, C.P. 6128, Succ. Centre-ville, Montréal, H3C 3J7, Québec, Canada
[12] Constellation, 1310 Point Street, Baltimore, MD 21231, USA
[13] Space Science Institute, 4765 Walnut Street, Suite 205, Boulder, CO 80301, USA

ABSTRACT

White dwarfs with metal pollution are caused by the accretion of rocky dust from tidally disrupted minor bodies and are signposts for planetary systems. These minor bodies are perturbed by planets that have survived post-main sequence evolution. Open questions exist as to the typical mass of the perturbers and the specific planetary architectures that cause metal pollution. JWST's sensitivity in the mid-IR has opened new doors to deciphering polluted white dwarfs. We present JWST Cycle 1 MIRI imaging of four nearby metal-polluted white dwarfs with the goal of detecting and characterizing planetary companions. With deep mid-IR imaging we are sensitive to cold Jupiter-mass planet analogs. In addition to finding two candidate planetary companions, for the first time we detect significant excesses above the expected photospheric emission at 21 μm for two of our targets, WD 2149+021 and WD 2105-820. WD 2105-280 has a candidate planetary companion at a projected separation of 34 au and an infrared excess–if both candidates are confirmed, it would represent the first WD multi-planet system. We investigate whether these excesses could be caused by very low luminosity warm dust disks or planets. While both are likely, we argue that the most likely explanation for the excesses is that they are the thermal emission from jovian-mass planets in orbits with semi-major axes <10 au, using a combination of observational constraints. If most of the candidate planets presented here are confirmed, it would suggest that metal polluted white dwarfs are frequently orbited by at least one giant planet.

Keywords: White dwarf stars(1799), Exoplanets(498), Circumstellar disks(235), James Webb Space Telescope(2291)

1. INTRODUCTION

The ultimate fate of our Solar System is one of the fundamental questions asked by humanity. While there is no path for us to directly observe the death of our own Solar System billions of years in the future, we can nevertheless

turn to astronomical observations to create a basic picture of how things might proceed both for terrestrial planets, giant planets, and the associated minor bodies and moons that fill out the known Solar System.

Studying the evolution of planetary systems at the extremes of planet survivability is a useful tool for gaining more insight into the architecture and chemistry of planetary building blocks around main sequence stars. Just as the careful pathologist can study a human body to determine a person's life and habits, so too can astronomers sift through the wreckage of past planetary systems to learn how they are formed. It turns out that careful observation of the end states to main sequence evolution, white dwarfs (WDs), provide many helpful and sensitive avenues to this pursuit.

Even before WDs were recognized as the corpses of solar-type stars, evidence of atmospheric pollution had been identified (van Maanen 1919). The first spectroscopy of WDs occasionally showed Ca absorption features, earning them the designation of DAF or DAwk (Eggen & Greenstein 1965). These discoveries were initially attributed to accretion from the interstellar medium (ISM) (Dupuis et al. 1992) or radiative levitation in hotter WDs. The advent of visible echelle spectroscopy with large telescopes (e.g. Zuckerman et al. 2003) and UV spectroscopy (e.g. Koester et al. 2014) with the Hubble Space Telescope revealed a significant occurrence of metal pollution around WDs, with over 25% of WDs showing some level of pollution and that by and large the abundance patterns of the pollution are consistent with rocky bodies as opposed to the ISM (Xu et al. 2014, e.g.).

The launch of the James Webb Space Telescope allows a new window into the fate of planetary systems. The MIRI Imager (Bouchet et al. 2015; Dicken et al. 2024) is sensitive enough to detect cold giant planet companions to WDs (Limbach et al. 2022; Mullally et al. 2024; Limbach et al. 2025) and small amounts of dust (Poulsen et al. 2024). Giant planets are detectable via both infrared excess and resolved companions, while dust is observed as an infrared excess, since WD dust disks are very compact and reside close to the Roche tidal disruption radius of the host star ($R \sim 1\ R_\odot$).

As part of an exploratory JWST Cycle 1 Program (PID 1911 PI: S.Mullally Mullally et al. 2021), we searched four nearby metal-polluted WDs with no known IR excess for evidence of planetary companions or debris. Despite a small sample size, three of the four WDs show interesting evidence for planets or dust, suggesting that further observations with JWST could reveal a wealth of information about planetary systems that are past their prime.

In §2 we discuss the four WD targets, while in §3 we detail the observational program and report precise mid-IR photometry and imaging of these WDs beyond 12 μm for the first time. In §4, we detail direct imaging searches for resolved substellar companions to the four WDs, placing stringent limits to the presence of giant planets in orbits beyond $\sim$10 au. In §5 we report excesses around two of the four WDs and determine the most likely interpretation as two candidate unresolved planets in orbit around WD 2149+021 and WD 2105-820 in §6. Finally we discuss our results in §7.

2. THE WD SAMPLE

The four WDs were selected to contain evidence of metal pollution from at least one atomic species, be nearby to the Earth, and have a total system age less than that of the Earth to ensure a sensitivity to giant planets with the least amount of observing time. We list details of the targets in order of decreasing distance from the Earth, and report our derived fundamental parameters in §3.1. A brief history of WD 2149+021 was already presented in Poulsen et al. (2024), so we skip that object.

2.1. *WD 2105-820*

WD 2105-820 was reported as a WD in Luyten (1949). It was identified early on as a potentially good target for directly imaging giant planets (Burleigh et al. 2002) and was soon found to have a detectable Ca line (Koester et al. 2005), indicative of active rocky material accretion. It was discovered to have a $\sim$9kG magnetic field (Landstreet et al. 2012), and further measurements imply that it is consistent with a simple dipole with a magnetic axis that is roughly aligned with the rotation axis (Bagnulo & Landstreet 2018). Interestingly, there is evidence that such a magnetic field can suppress convection in the upper atmosphere of this WD, which might have implications for the inferred accretion rate of metals and does slightly modify the inferred fundamental parameters of this target (Gentile Fusillo et al. 2018). Mullally et al. (2024) reported a candidate planet between 1-2 $M_{\rm Jup}$ around this WD at a projected separation of 34 au.

2.2. *WD 1620-391*

WD 1620-391 was first discovered to be a DA WD via photographic plate spectra under the name CD-38°10980 (Stephenson et al. 1968). It was recognized as a possible common proper motion companion to HR 6094, which was

later confirmed. HR 6094 is also host to a Jupiter analog exoplanet companion in a 1.32 au orbit (Mayor et al. 2004). It was the third WD to have an estimate of its gravitational redshift (Wegner 1978), and is constrained to have a magnetic field of <7.8kG (Kawka et al. 2007). At a distance of 12.911±0.007 pc, it is one of the closer hot WDs, making it amenable to studying both its EUV and X-Ray emission (e.g. Marsh et al. 1997). The local ISM G cloud is in this direction of the sky and has a projected heliocentric radial velocity of -25 km s^{-1}, well separated from the observed heliocentric radial velocity of the WD (v=44.0±0.6 km s^{-1})(Malamut et al. 2014; Napiwotzki et al. 2020). WD 1620-391 has also been used as a target for previous direct imaging searches for planets in the NIR and mid-IR with HST and Spitzer (Debes et al. 2005; Hogan et al. 2009), with no compelling companions or excesses detected (Debes et al. 2007).

WD 1620-391's status as a DAZ has historically been muddied in the literature. Optical echelle spectroscopy shows no obvious Ca H or K lines, nor are any trace metal lines obviously detected. UV observations from IUE (International Ultraviolet Explorer) in particular seemed to show only circumstellar velocities for transitions of Si due to a difference between the observed line centers and that of hydrogen lines in the visible (Holberg et al. 1995). FUSE (Far Ultraviolet Spectroscopic Explorer) observations of WD 1620-391 showed the presence of Si III lines near 1100 Å that were consistent with a photospheric origin; an assumed log Si/H abundance of -7.69 in the atmosphere predicted consistent equivalent widths in Si for both the FUSE and the IUE spectra(Wolff et al. 2001). These authors could not reconcile the possible velocity differences to that expected in the photosphere. Given that the IUE data measured the radial velocity of the ISM components to be -30 km s^{-1}, the most likely explanation is that there was a $+5$ km s^{-1} velocity offset in the IUE data. When that is accounted for, the average velocity of the reported circumstellar components is 44 km s^{-1}; in line with the latest photospheric RVs derived from optical echelle spectroscopy (Napiwotzki et al. 2020). We thus consider WD 1620-391 a bonafide DAZ.

To definitively confirm this, we obtained the Hubble Advanced Spectral Products (HASP) Space Telescope Imaging Spectrograph (STIS) UV echelle spectra of WD 1620-391, which includes data from HST program ID 14076 (PI: Gaensicke; E140M, E230M Debes et al. 2024). We focused our attention on the species reported in the IUE data and verified whether they were detected, and measured their radial velocities. We obtained a Gaussian fit to each of 20 candidate photospheric lines and 15 ISM lines, obtained the best fit line center, and then calculated a radial velocity from those fits. The mean value and the standard deviation in measured velocities from the STIS data for the ISM components is -26.6±1.8 km s^{-1}. All of the non-ISM lines reported in Holberg et al. (1995) were also strongly detected in the STIS observations and the mean of their velocities was 43.52±1.3 km s^{-1}. Both values are consistent, within the uncertainties, to previous determinations of the ISM velocity in this line of sight and to the radial velocity of WD 1620-391 as determined in the visible, confirming that active rocky accretion is occurring.
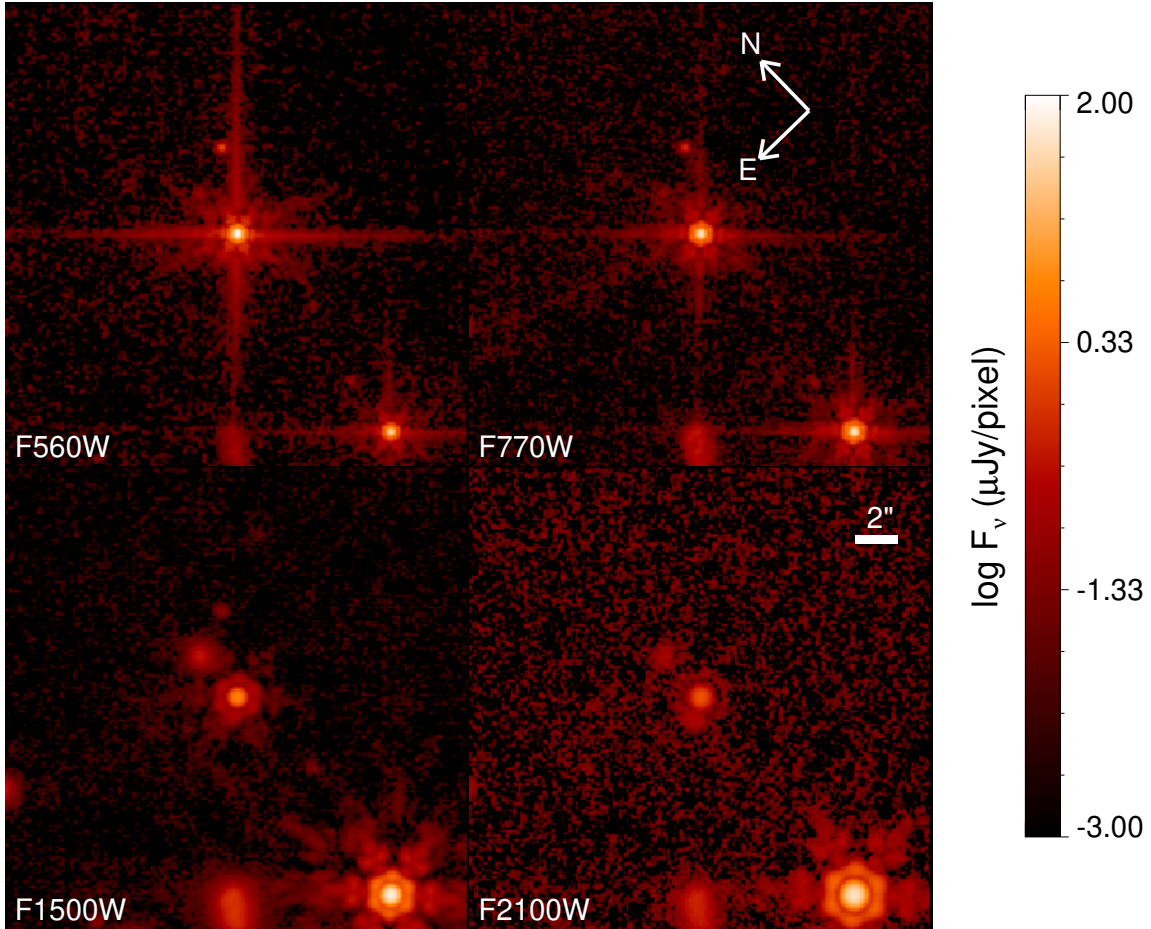
2.3. *WD 1202-232*

WD 1202-232 was first identified as a DA as part of the Edinburgh-Cape Survey (Kilkenny et al. 1997), and then was noted to have Ca metal line absorption shortly after its discovery (Zuckerman et al. 2003; Koester et al. 2005). It has been searched for magnetic fields but no significant field was detected (Jordan et al. 2007; Bagnulo & Landstreet 2018). Low resolution spectroscopy from the UV through the near-IR has been obtained for this target with HST as part of the CALSPEC series of high quality spectrophotometric stars (Bohlin et al. 2014), and a candidate planetary companion between 1-7 M$_{\rm Jup}$ was reported in Mullally et al. (2024) at a projected separation of 11 au.

3. OBSERVATIONS

JWST program ID 1911 targeted the WDs with the mid-infrared instrument (MIRI) in full readout, imaging mode with four different broadband filters: F560W, F770W, F1500W, F2100W. The observations' exposure times were designed to make it possible to directly image planets with masses greater than or equal to 1 Jupiter mass orbiting the WD with the 15 μm filter. The 21 μm filter exposure was set to ensure a signal to noise of 55 in order to detect unresolved planets larger than one Jupiter mass using infrared excess. The short exposures of the 5 and 7 μm filters were intended to reject false-positive detections of non-planetary resolved companions, and to measure the white dwarf photospheric brightness against which flux excesses from unresolved companions can be detected. For each filter a 4, 8 or 12-point dither in the cycling pattern were used: a 4-pt pattern for the short F560W and F770W observations, a 12-pt pattern for the deep F1500W observations of WD 2105-820 and WD 2149+021 and a 8-pt pattern for all the rest.

The images were processed using build 11.1 (data processing software version 2022_5b and calibration software version of 1.16.0) of the JWST Calibration pipeline starting from the uncal files, using a CRDS context from jwst_1293.pmap

**Figure 1.** The four MIRI images of WD 1202-232. Each field represents $22'' \times 22''$ with the WD at the center.

and CRDS version of 11.18.4. Each set of images was processed through stage one (calwebb_detector1) and two (calwebb_image2) of the imaging pipeline using mostly default parameters. The only non-default values set were in the jump step of the calwebb_detector1 pipeline. For that step, we set the rejection threshold to 5 σ rather than the default of 4, and turned off the cosmic ray shower finding code, using only the standard jump detection algorithms. After the stage two pipeline was run, a median background image was created from the stacked _cal.fits images for each filter and subtracted from each cal file. Lastly, the level three imaging pipeline (calwebb_image3) was run on the background subtracted files and combined with the resample kernel set to 'square', the resample weight_type set to 'exptime', and the outlier detection 'scale' values being set to (1.0 and 0.8), which is twice the default values, but using the standard parameter reference files for all other parameter settings. These background subtracted cal and i2d files were used for all subsequent analyses.

Most of the updates for the build 11.1 pipeline were minor bug fixes and code cleanup like ensuring consistency between the SCI, ERR and DQ extensions of the data to make sure that a pixel flagged as DO_NOT_USE in the DQ extension would be flagged as a bad pixel and not used in the SCI and ERR arrays. These updates would not have had a large effect on the data from previous versions of the pipeline, though there may have been a few more Not a Number valued pixels in the calibrated files before combination in the (calwebb_image3) pipeline.

Figures 1 to 4 show $22'' \times 22''$ fields surrounding each WD target in the four filters. With the exception of WD 1620-391, the fields contain a mix of galaxies of varying morphology and a smattering of point sources. Since WD 1620-391 is close to the galactic plane (b=+7.3 degrees), some spatially variant galactic cirrus is most noticeable at 7 and 15 μm, complicating the fidelity of the background subtraction and decreasing our sensitivity to faint point sources in localized regions.

3.1. *White Dwarf Photometry*
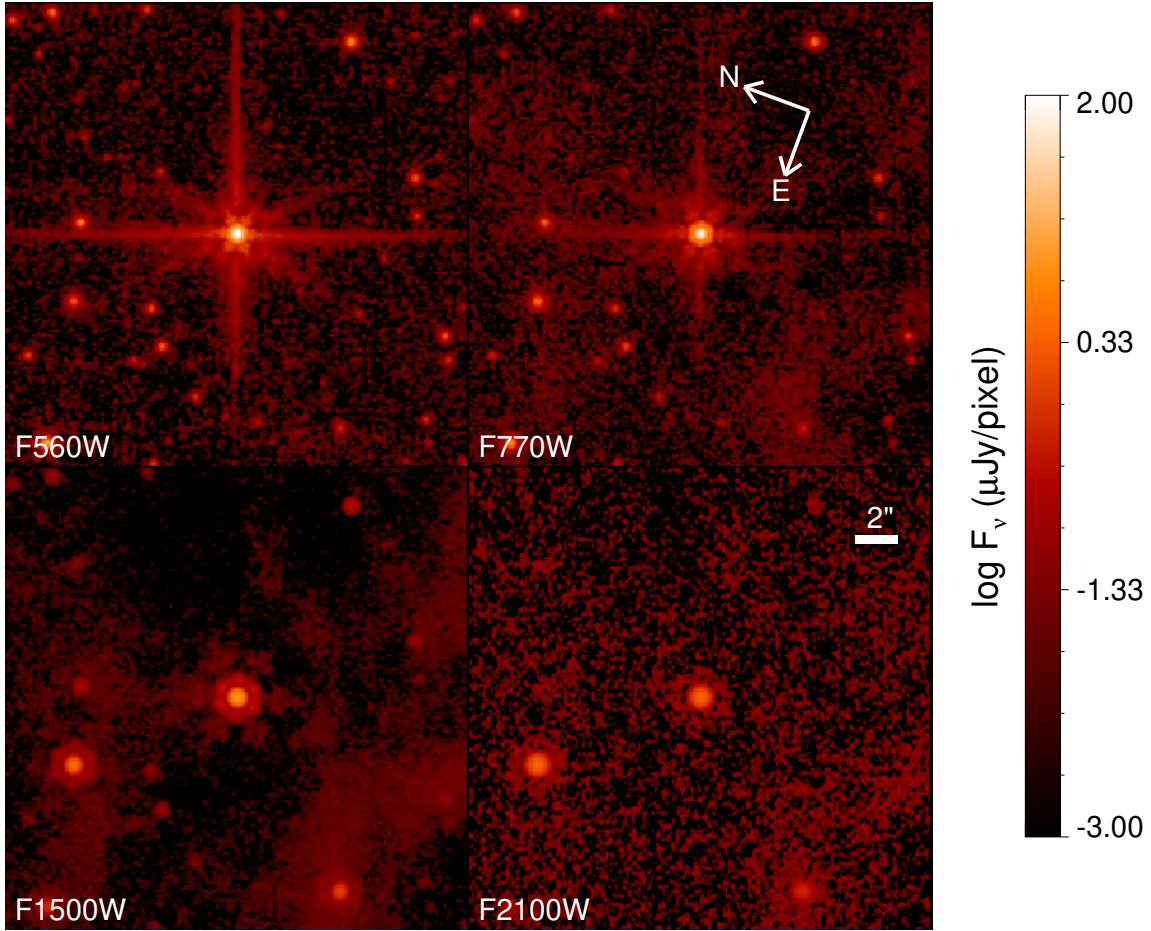
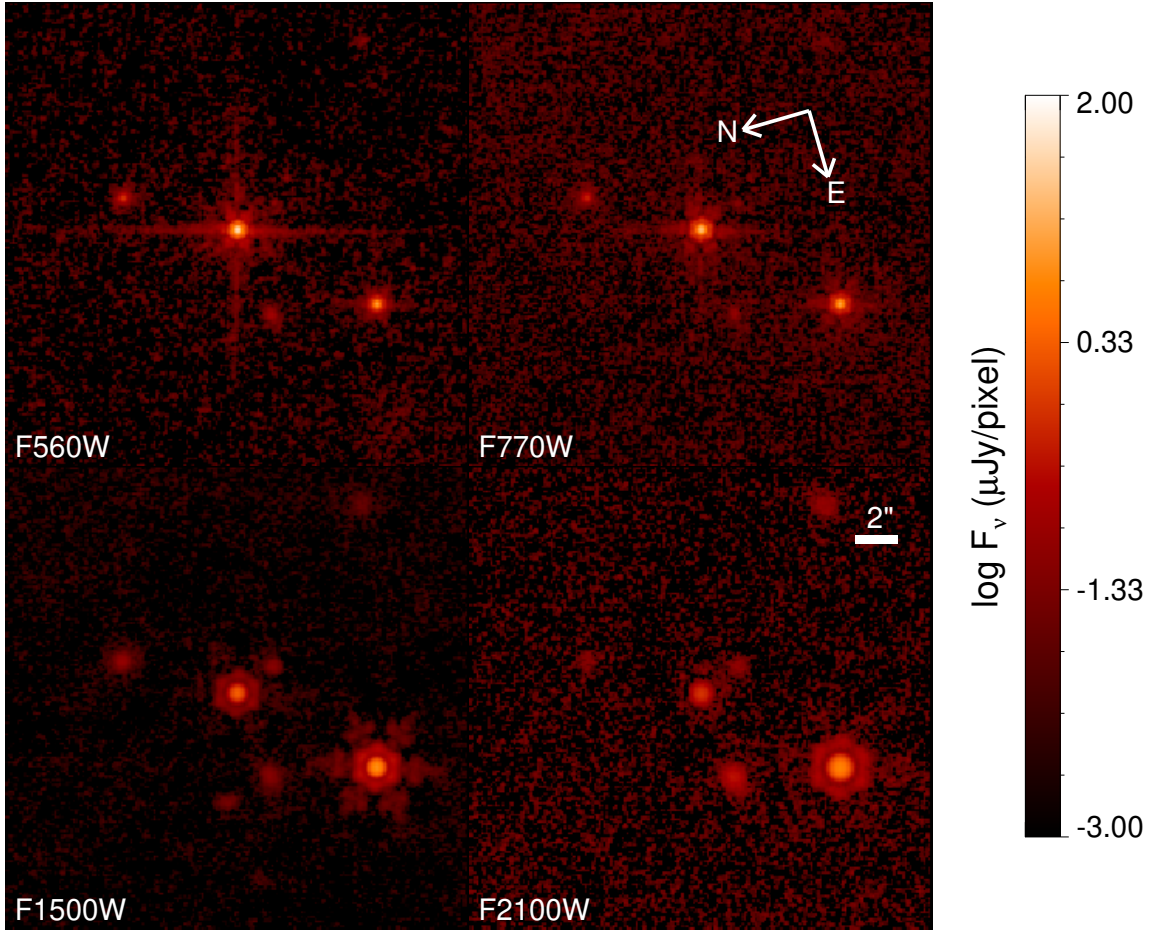**Figure 2.** The same as Figure 1 but for WD 1620-391.

Postage stamp images from the dither-combined images were created of each WD to ensure that aperture photometry could be performed to match the procedure obtained for the MIRI absolute flux calibration (Gordon et al. 2025). The default aperture sizes and background annuli for each filter that corresponded to 70% enclosed energy was derived using the aperture correction file jwst_miri_apcorr_0014.fits located at the JWST CRDS website[1]. We made use of the IDL routine *aper.pro* part of the IDL Astronomy Users Library[2]. Based on this approach, our photometry should be accurate to ∼2%, with this uncertainty dominated by any systematic uncertainties between our predicted photospheres and the observed photometry. In §3.3, we look more deeply into what our likely systematic uncertainties might be.

In addition to the JWST photometry we compiled visible and Near-IR photometry for each WD, similar to the procedure for WD 2149+021 detailed in Poulsen et al. (2024). For WD 2105-820, we made use of GALEX (Bianchi et al. 2017), Sloan $g/r/i/z$, APASS DR9 B/V, Gaia DR3 G/G_{BP}/G_{RP}, 2MASS J/H/K, ALLWISE W1/W2/W3, and Spitzer IRAC1, IRAC2, IRAC3, IRAC4 SEIP fluxes. We obtained a best fit T_{eff}, log g based on the Gaia parallax and a chi-square minimization against the publicly-available cooling models provided by P. Bergeron (Holberg & Bergeron 2006; Bédard et al. 2020) and report the results in Table 2. WD 1202-232 also has an empirical CALSPEC spectrum, and as mentioned previously, these spectra have absolute flux accuracies that approach 1%. To that end, we convolved the CALSPEC spectrum, which spans the FUV to the Near-IR, into the GALEX and Sloan $g/r/i/z$ filters using the Spanish Virtual Observatory SPECPHOT tool[3]. WD 1620-391 possesses a high SNR STIS/E140M+E230M spectrum that we used to calculate synthetic GALEX photometry, as it is too bright for accurate GALEX fluxes. Some bands were ignored due to possible saturation, contamination from atmospheric extinction such as the Sloan u, possible

---

[1] https://jwst-crds.stsci.edu/

[2] https://github.com/wlandsman/IDLAstro

[3] http://svo2.cab.inta-csic.es/theory/specphot/

Figure 3. The same as Figure 1 but for WD 2105-820.

contamination from background sources such as W3, or in the case of WD 2105-820, GALEX fluxes were ignored to better approximate the magnetic radiative model required, which produces different photospheric fluxes in the UV compared to a standard non-magnetic convective model (Gentile Fusillo et al. 2018).

3.2. *Procedure for predicting JWST MIRI Fluxes*

The publicly available Bergeron cooling models do not have predictions for any of the MIRI bands, and thus we took the best fit WD parameters and used them to generate high resolution photospheric models specific to each WD that extended to 30μm. We first scaled the photospheric model by the best fit radius and distance, and then further scaled these spectra to existing CALSPEC or STIS UV spectra. WD 2105-820 was not corrected at this step. In general this second step changed things by less than 1%.

Then, taking the publicly available MIRI filter transmission profiles from the Spanish Virtual Observatory Filter Service (Rodrigo et al. 2024) we convolved the models with each profile to create an accurate prediction of the MIRI flux in each band (Holberg & Bergeron 2006).

Figures 5 to 8 show the resulting spectral energy distributions (SEDs) for each of the four WDs compared to both the Bergeron photometric predictions (red asterisks), the extended photospheric spectral models (black lines), the observed archival photometry (black squares), and the new MIRI photometry (blue large squares). A comparison between observed and predicted flux in each filter bandpass is also shown in the lower panel of each figure with ± 3-σ boundaries denoted as dashed lines.

Table 1. Photometry of the target WDs

Filter	WD2149 Flux	WD2105 Flux	WD1620 Flux	WD1202 Flux
	μJy	μJy	μJy	μJy
GALEX FUV	50000± 500		524725± 15741	184± 1
GALEX NUV	39799± 397	6309± 174	341963± 10258	8408± 84
g′	32342± 646		26507± 530	
r′	23816± 476		27051± 541	
i′	18241± 364		25528± 510	
z′	13836± 276		22731± 454	
U			216796± 3993	
B	33025± 1247	11440± 579	181654± 3346	24257± 670
V	28250± 1717	13274± 501	143689± 2646	28094± 776
R			107916± 1987	
I			74661± 1375	
G_{BP}	28258± 565	11769± 235	152455± 3049	25092± 501
G	25157± 503	11712± 234	129139± 2582	26053± 521
G_{RP}	17269± 345	10122± 202	82503± 1650	24551± 491
J	8365± 184	6475± 155	37298± 721	17477± 386
H	4964± 169	4264± 129	21237± 449	12311± 306
K_s	2918± 99	2582± 92	13085± 265	7726± 185
W1	1369± 31	1278± 29	5596± 118	3660± 84
W2	764± 22	703± 19	2793± 59	1985± 43
W3		236± 105		643± 138
IRAC1			4975± 149	
IRAC2	786± 23	727± 21	3119± 93	2033± 60
IRAC3			1974± 59	
IRAC4	272± 8	256± 7	1076± 32	700± 21
F560W	508 ± 10	463 ± 9	2030 ± 41	1304 ± 26
F770W	282 ± 6	262 ± 5	1112± 22	726 ± 14
F1500W	73 ± 2	71± 1	277 ± 6	183 ± 4
F2100W	43 ± 1	42± 1	145 ± 3	103 ±2

Table 2. Fundamental parameters of the target WDs

	WD2149	WD2105	WD1620	WD1202
d(pc)	22.56±0.02	16.179±0.004	12.91±0.01	10.427±0.002
T_{eff} (K)	17840±160	9890 K[a]	24700±600	8720±120
$\log g$	8.01±0.01	8.20±0.03[a]	8.04±0.03	8.00±0.04
M ($M_\odot$)	0.62±0.01	0.7±0.06	0.64±0.01	0.6±0.03
t_{cool} (Gyr)	0.114±0.003	0.83±0.1	0.026±0.004	0.90±0.07
t_{MS} (Gyr)	$2.9^{+3.7}_{-1.3}$	$1.6^{+0.8}_{-0.24}$	$2.18^{+3.04}_{-0.84}$	$5.24^{+5.04}_{-2.50}$

[a]Based on the parameters determined in Gentile Fusillo et al. (2018)
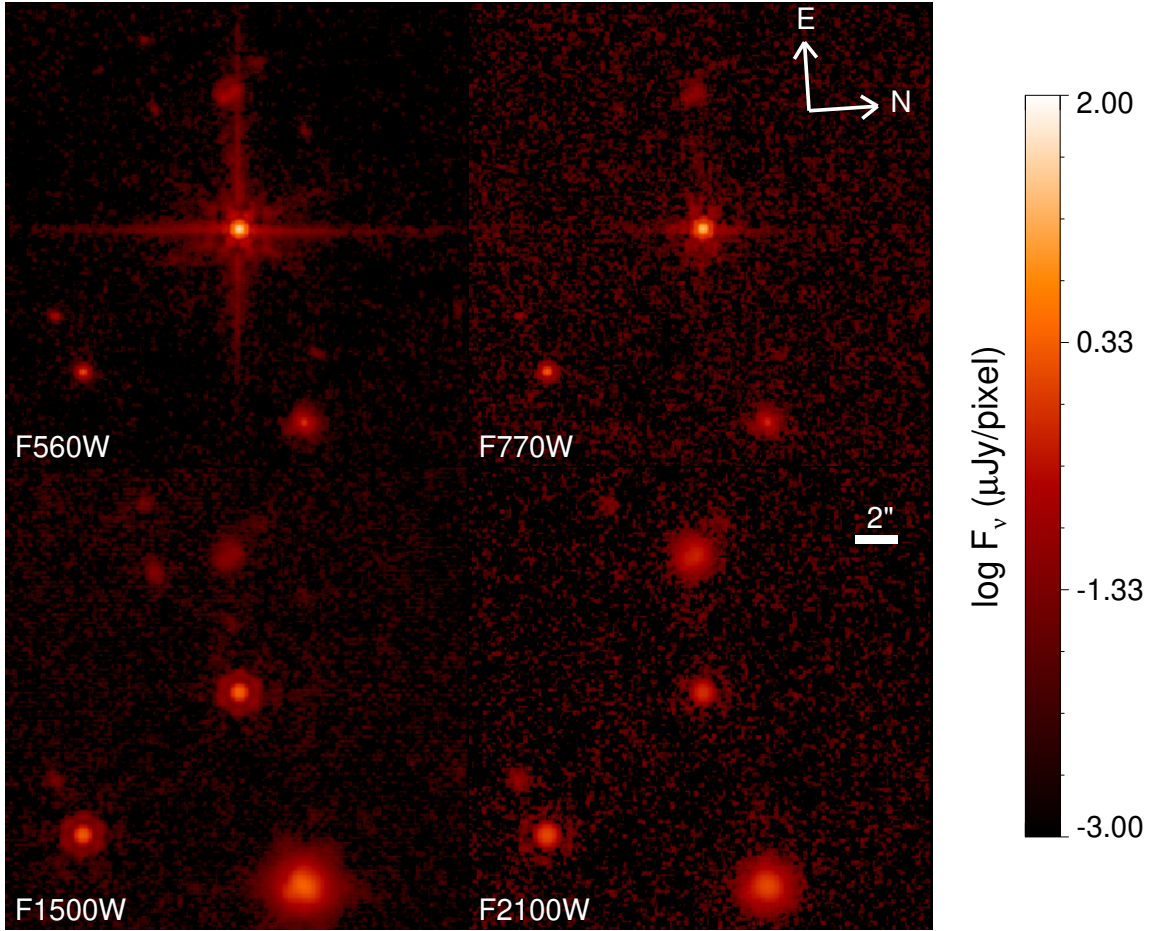
Figure 4. The same as Figure 1 but for WD 2149+021.

3.3. *Photometry match to the models*

When we compare the WD model photospheres to the observations we find that WD 1620-391 and WD 1202-232's photometry match to within 3-σ across all wavebands, including the JWST MIRI filters, with the assumption of 2% systematic uncertainties combined with the existing photometric uncertainties. For WD 2105-820 and WD 2149+021, we find a similar match across all wavebands except for their F2100W photometry, which deviate from the models significantly by 5.6 and 5.1 σ respectively. Additionally, both targets' F1500W photometry is elevated at 2.0 and 1.2 σ, respectively. See Figures 7 and 8.

To estimate our systematic photometric uncertainties, we try to replicate the procedures adopted for the absolute flux calibration of MIRI (Gordon et al. 2022), we also downloaded archival data and CALSPEC models of JWST WD calibration standards (Gordon et al. 2022), G191-B2b (F560W, F770W, F1500W), LHS 749b (F560W, F770W), GD 71 (F560W, F770W), GD 153 (F560W, F770W), and WD 1057+719 (F560W, F770W). To supplement F1500W, we included three F1500W images of the brightest DAs from the MEAD survey and created our own models for them: WD 0839-327, WD 0752-676, and WD 0644+375 (Program 3964, PI:Poulsen). Since none of the WD standards had F2100W images, we also inspected three individual full frame F2100W observations of BD+60-1735, as well as a SUB64 F2100W observation of 10 Lac, μ Col, and λ Lep, all part of the hot stars sample from Gordon et al. (2022). We also included an F2100W observation of WD 0644+375 from the MEOW survey (Program 4403, PI: Limbach). This ensured we had between 7 and 10 independent measures of MIRI flux in all four filters compared to at least 7 different expected model photospheres. In every filter except F2100W our sample was derived from only white dwarfs, with F2100W using a sample with half white dwarfs and half hotter stars.

In the case of LHS 749B, the F560W flux measured for this star was anomalously low compared to the best guess model. This could be due the possibility that for some of the images smaller dither offsets were used, which can increase

negative flux residuals at the sky subtraction step of calibration. Additionally, there is evidence that LDS 749B is fainter than expected around 5 μm in NIRSPEC calibration data, indicating the possibility of additional atmospheric opacity that the current best model for the star does not include (C. Proffit, private communication). We did not include the F560W photometry from LDS 749B in our estimates below.

We then performed the same aperture photometry for all of the calibration targets and our targets (with the exception of the excess candidates in F2100W and WD 2105-820 in F1500W) and calculated the mean and RMS of the measurements, which provides the statistical plus systematic uncertainties in an individual measurement of absolute flux for a given target.

Figure 9 shows our resulting independent test of the JWST absolute flux calibration for these MIRI filters. We see an excellent match, in line with an object-to-object RMS of ∼2%. We found that the average ratio of observed photometry to photosphere prediction was 1.00±0.02 for F560W (8 targets; 8 measurements); 1.01±0.02 for F770W (7 targets; 7 measurements); 1.00±0.02 for F1500W (7 targets; 7 measurements); and 1.00±0.02 for F2100W (7 targets; 10 measurements). This excellent agreement across a factor of ∼10 in effective temperature for the WDs suggests that it's highly unlikely that the excesses we measure in the F2100W filter are spurious or due to uncertainties in the absolute flux calibration of JWST or in the models of these well understood WDs.

Another possibility is that the MIRI time-dependent sensitivity was somehow incorrectly applied during the period of time that our WD targets were observed at F2100W, resulting in a subtle systematic offset in the expected flux[4]. The declining sensitivity was modeled as an exponential decline with time during Cycle 1 and 2. We find the possiblity that an incorrect sensitivity correction is responsible for our observations to be highly unlikely. First, if this were due to a trend in the sensitivity correction, we would expect to see that the excess observed would be correlated with observing epoch. This is not the case–WD 2149+021 was the first WD observed, and WD 2105-820 was the last one. To further investigate this, we measured the photometry of BD+60-1735, which was observed a total of six times within a few months of our WDs in F2100W (See Figure 10). With the exception of the excess WDs, the median ratio of observed to model fluxes was 0.985±0.013, consistent with no systematic trend over time. Thus we expect the sensitivity correction to add negligible uncertainty to our F2100W photometry.

We note that Poulsen et al. (2024) did not make a claim for a signficant excess at F2100W for WD 2149+021. This is because for that work they assumed an interpolation between predicted fluxes in the WISE bands rather than computing a full spectral resolution model that could be convolved with the JWST filter transmission curves. We determined that the previous approach overestimates the mid-IR WD continuum by 5-10%, which we confirmed in tests with G191-B2b at 10 and 15 μm. This was enough to suppress the long wavelength excess that is present relative to the uncertainties.

Irrespective of the flux calibration factors, relative fluxes bewteen two WDs of similar $T_{\rm eff}$ should be nearly constant in the MIRI filters. We first compare the ratio of WD 2105-820's flux to WD 1202-232's flux. The ratios for F560W, F770W, F1500W, and F2100W are 0.354, 0.361, 0.386, and 0.409. The F2100W ratio is 15% higher, similar to the excess seen relative to WD 2105-820's model. WD 2149+021 and WD 1620-391 are hotter WDs, their ratio is 0.251, 0.254, 0.265, 0.302 for F560W, F770W, F1500W, and F2100W. WD 2149+021's F2100W ratio is 20% higher than at shorter wavelengths as well.
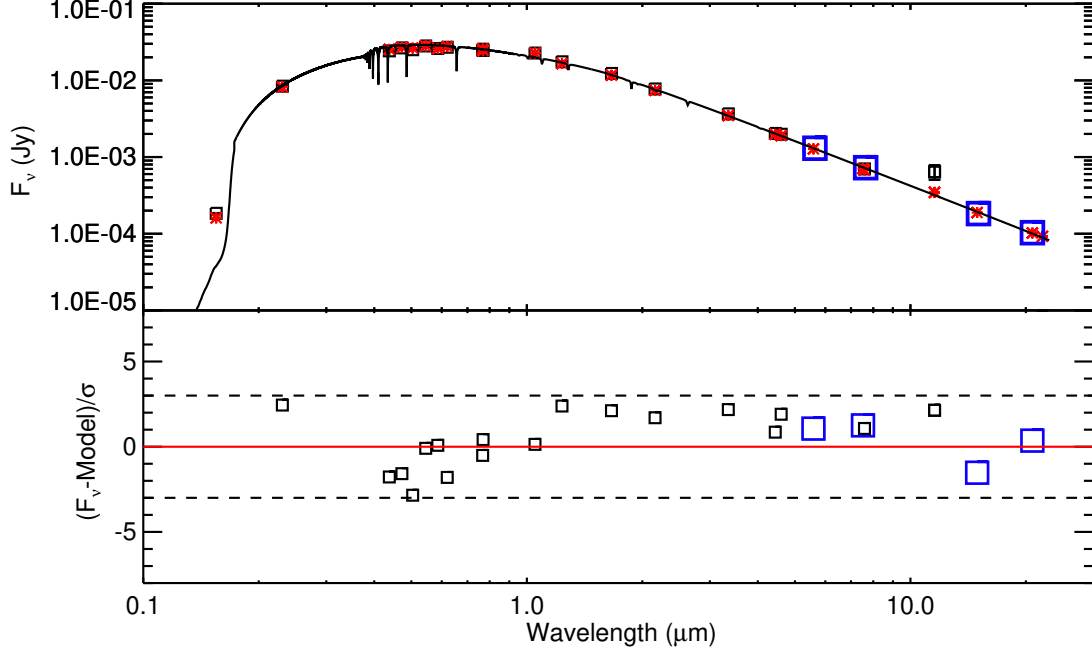
3.4. *PSF Subtraction*

We used the same procedure for PSF subtraction as detailed in Poulsen et al. (2024) and Mullally et al. (2024). Briefly for each WD a 15 μm reference PSF was constructed from an average of WD 1620-391, WD 2149+021, and WD 2105-820 (removing whichever WD was the target) with background sources masked out. The reference PSF was shifted and scaled to match the target WD and subtracted. The images were inspected for significant point sources and all candidates found within a projected physical separation of 100 au had their photometry measured. Anything with a F1500W/F560W ratio >1 and a FWHM within 20% of the expected F1500W FWHM was considered a possible planet candidate.

3.4.1. *Searching for Planets with Kernel Phase Imaging*

Kernel phase imaging (KPI) is an analysis technique that generalizes the concept of aperture masking interferometry to full pupil imaging (regular images), enabling probing for companions at roughly half the traditional diffraction limit

---

[4] https://jwst-docs.stsci.edu/jwst-mid-infrared-instrument/miri-performance/miri-sensitivity#gsc.tab=0

Figure 5. (top panel) Spectral energy distribution of WD 1202-232 and comparison to its predicted photospheric emission. The black line represents the model photosphere for the WD, the red asterisks are the predicted model fluxes in a given filter, and the black squares are archival photometry for the WD (See Table 1). The blue squares represent the observed JWST fluxes in F560W, F770W, F1500W, and F2100W. (bottom panel) Residual photometry relative to the model photosphere, weighted by the photometric uncertainties. The black squares are archival photometry, while the blue squares represent the JWST photometry.
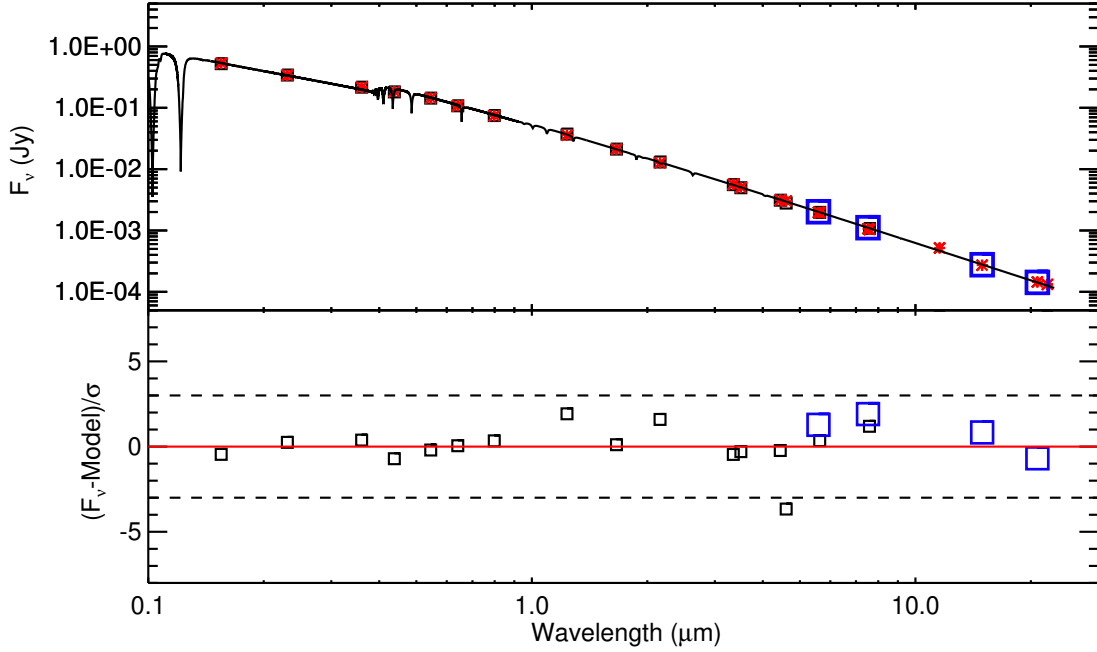

Figure 6. Same as Figure 5, but for WD 1620-391.
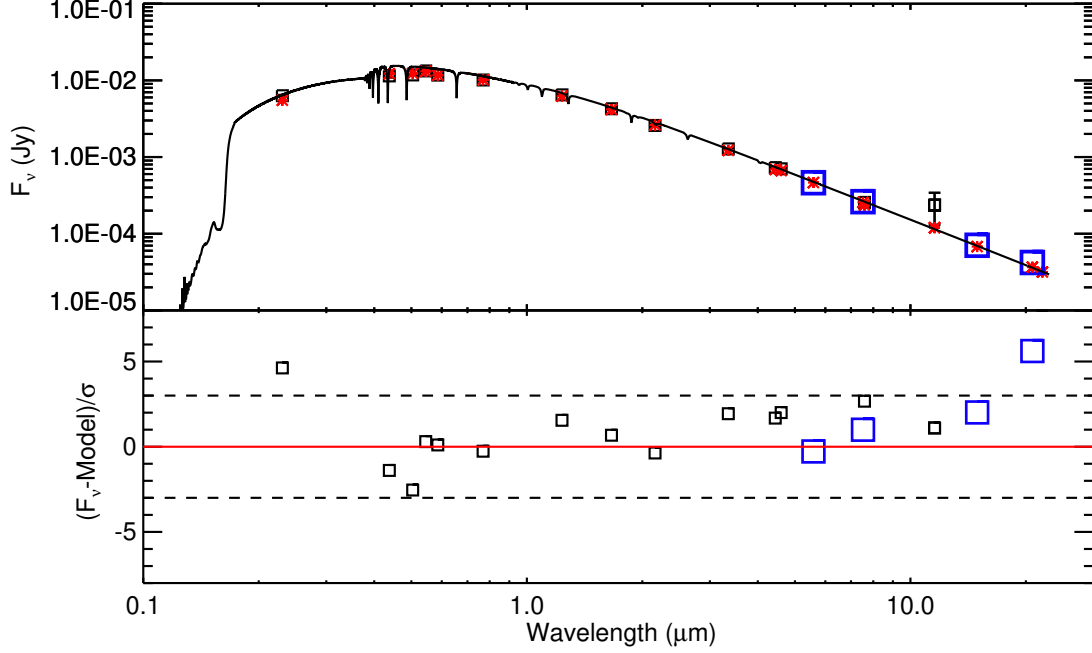
Figure 7. Same as Figure 5, but for WD 2105-820. Note the significant 5.6 σ excess at 21 μm. Additionally, there is a tenatative excess at 2.0 σ at 15 μm.
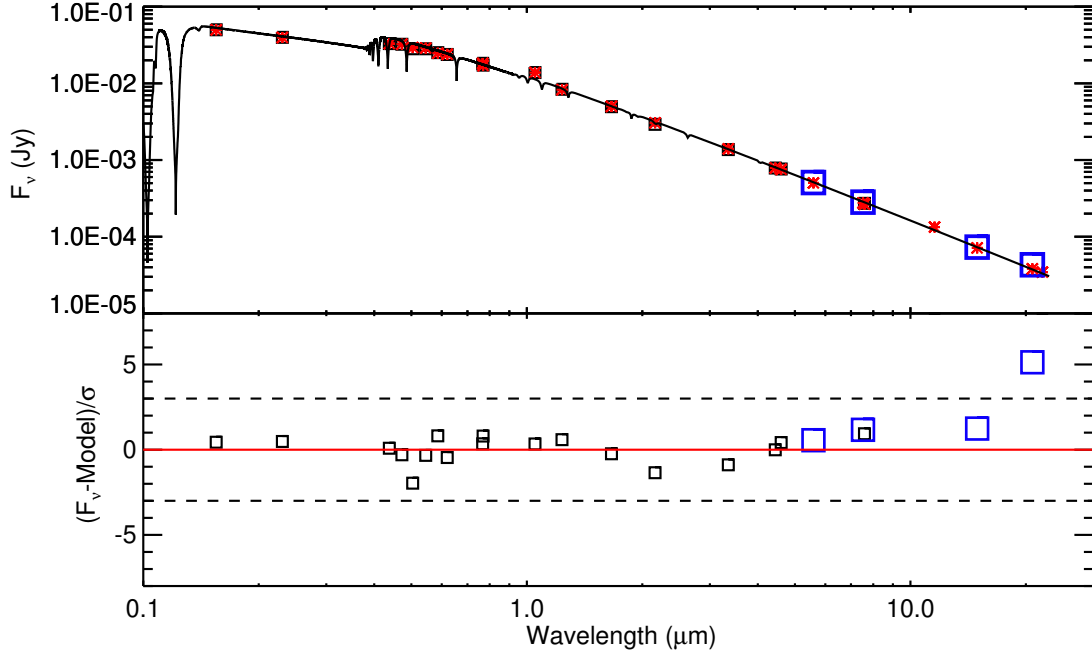
Figure 8. Same as Figure 5, but for WD 2149+021. Note the significant 5.1 σ excess at 21 μm.

(Martinache 2010). The technique performs well when searching for companions at moderate contrasts ($\leq 6-7$ mag) in the near infrared (Pope et al. 2013; Kammerer et al. 2019, 2023) but, here, we apply KPI for the first time in the mid-infrared with MIRI, in the F1500W filter for which exposure times were maximized.

A pupil model from *jwst-kpi* (Kammerer et al. 2023) built of 540 sub apertures distributed over 3 hexagonally-shaped rings for each primary mirror segment was adopted to sample interferometric baselines. The model optimized
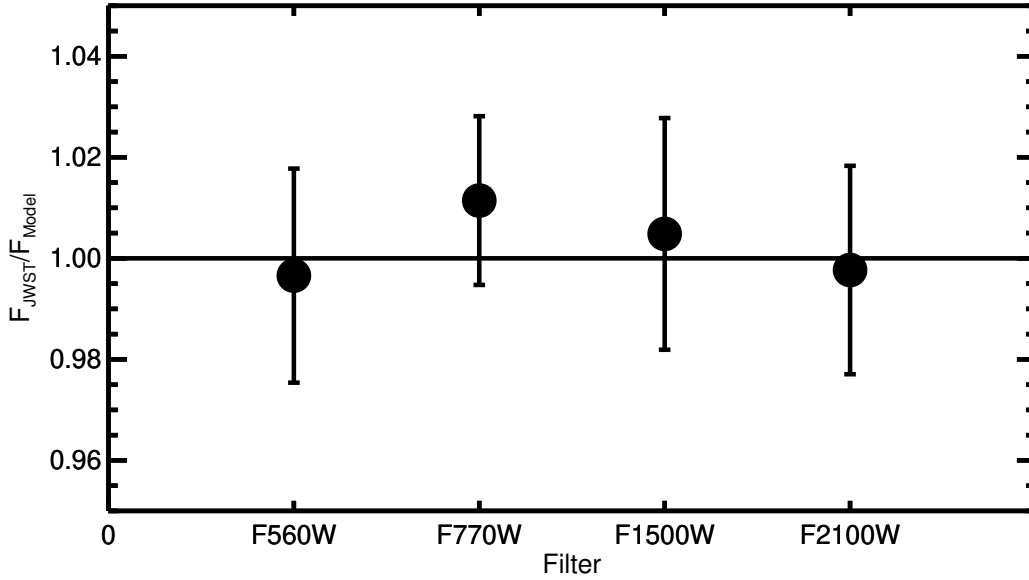
Figure 9. Comparison between the average measured flux in a given MIRI imager filter and the expected flux assuming the best-guess models for each calibrator star. Error bars are the calculated rms of each sample of stars, which indicates the systematic uncertainty due to stellar and white dwarf models.

for MIRI is tilted by 4.84 degrees to account for the MIRI aperture position angle and only retains pupil points yielding a minimum of 50 redundant baselines. KPI analysis was performed on cropped images of 51×51 pixels, or approximately $5''6\times5''6$, keeping in mind that KPI's sensitivity advantage is limited to $0.5\,\lambda/D$ ($0.25''$) $\leq$ separation $\leq\ \sim 2\,\lambda/D$ ($1.0''$). Figure 11 presents the 3σ contrast map produced in the KPI analysis of WD2149+021. For the 3 other targets, the map is very similar but scaled to different contrast ratios which correlate with the achieved point-source signal-to-noise.

4. RESOLVED PLANETARY COMPANIONS

Previous work has already investigated possible resolved companions around three of the WDs considered here, with high probability of $p > 98\%$ (Poulsen et al. 2024; Mullally et al. 2024). WD 2149+021 showed no high probability candidates, while WD 2105-820 and WD 1202-232 had high probability candidates. In this section we summarize the final contrast limits for each of our targets from a combination of direct imaging and KPI as well as report likely planet candidates within a projected separation of 100 au for each target.

Figures 12 to 15 show our 1-D contrast limits through a combination of our direct imaging and KPI techniques. The cross-over for both techniques is at approximately $0''5$, roughly at the spatial resolution limit for the F1500W filter. We convert the limiting flux ratios at F1500W, where we are most sensitive to resolved planetary companions, into masses based on the assumed mass, age, and distance to each target WD. We compare the contrast ratios to the recent detection of WD 1858+584b in F1500W (T_{eff}=184 K; M=5 M_{Jup}) (Limbach et al. 2025) and Jupiter's expected 15 μm flux ($T_{eff}\sim$150 K) scaled to the distance of each WD, which suggests our direct imaging with JWST/MIRI is sensitive to extremely cold giant planets even if our exact mass sensitivity is uncertain.

We searched each of the four targets for resolved point sources within a projected separation of 100 au (See Figure 16). We limit our search to this radius primarily because the probability of a coincident background point source with a red color (i.e. F1500W/F560W > 1) reaches close to unity beyond this projected separation (Poulsen et al. 2024; Mullally et al. 2024).

Our selection criteria for candidates were well detected sources at F1500W that possessed FWHMs consistent with an unresolved point source and an F1500W/F560W ratio >1. With these criteria we recover the two planet candidates reported in Mullally et al. (2024), but no other viable candidates.

4.1. *Limits to Resolved Planetary companions*
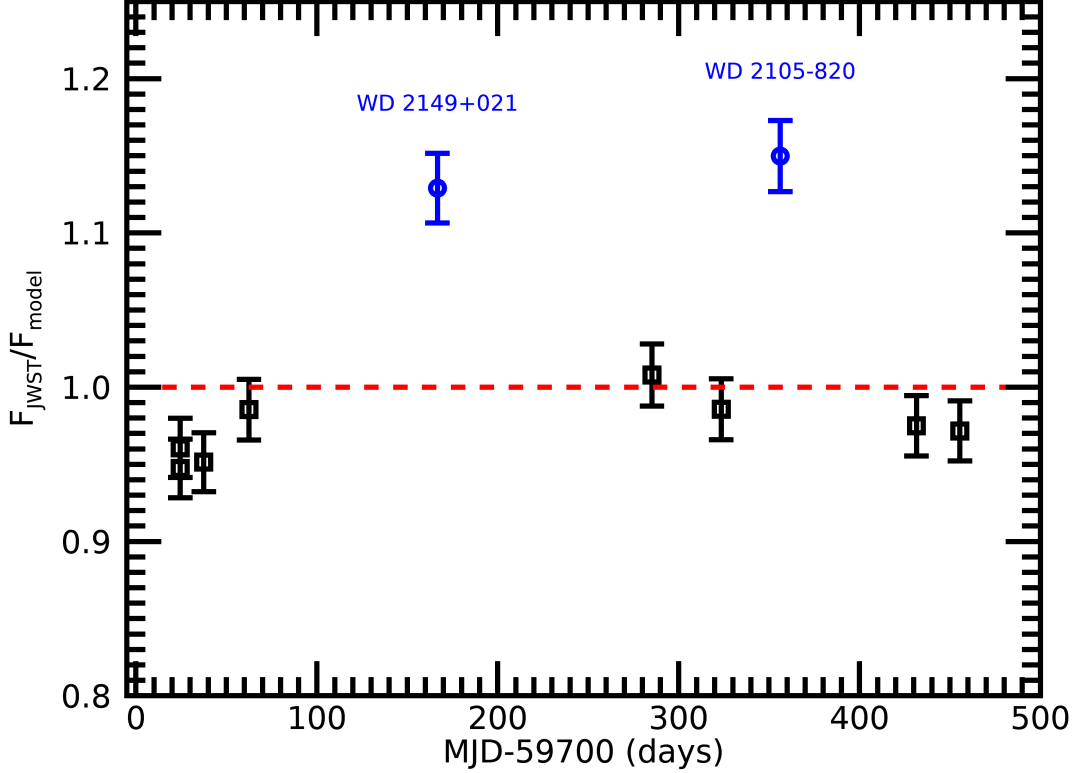
Figure 10. The ratio of observed flux in F2100W vs. time for calibrators and non-excess WDs (black squares) compared to our excess candidates (blue circles). The calibrator BD+60-1735 was observed starting around MJD 59700 with four epochs, and another two epochs were obtained around 480 days later. The GO 1911 targets were observed between MJD 59850 and 60100. The dashed line is a constant ratio of 1: the median of all observations is 0.985. The excess candidates are significantly above the constant ratio and there is no strong evidence for any systematic trends due to the sensitivity correction.

We calculated contrast curves in F1500W, the deepest images obtained for each WD, for the PSF subtracted images following the same procedures detailed in Poulsen et al. (2024). For the given total age of each WD ($t_{cool}+t_{MS}$, we used cloudless Sonora-Bobcat grid models (Marley et al. 2021) above 200 K and cloudless Helios grid models (Linder et al. 2019) below 2 M_{Jup}. We first calculated the proper T_{eff}, $\log g$ combinations for a given age corresponding to various substellar companion masses from the Sonora-Bobcat grid, and then computed them for the youngest and oldest age as defined by the uncertainties in Table 2.

We then interpolated JWST fluxes from the grids of predicted fluxes for ages between 1.5-10 Gyr. For the Helios grid, fluxes for specific ages for 0.3, 0.5, 1, and 2 M_{Jup} were pre-calculated. We then converted the predicted fluxes or magnitudes to apparent fluxes accounting for the distance to each WD.

5. LIMITS TO UNRESOLVED PLANETARY COMPANIONS

For WD 1202-232 and WD 1620-391, the lack of any IR excess out to 21 μm provides a strict limit to any unresolved planetary companions. For these targets we took the 5 σ upper limit in flux at F2100W and compared these to the same planet isochrones as in Section 4 spanning the age uncertainties. For WD 2149+021 and WD 2105-820 we instead use the 3 σ upper limit in flux at F1500W to estimate limits to unresolved planets under the assumption that the excess at F2100W is due instead to dust. For WD 2149+021 we find an upper mass limit of $4.2^{+2.9}_{-1.3}$ M_{Jup}, and $1.8^{+0.8}_{-0.3}$ M_{Jup} for WD 2105-820. For the remaining two WDs, we find an upper mass limit of $2.4^{+1}_{-0.6}$ M_{Jup} for WD 1202-232 and $2.4^{+2.2}_{-0.9}$ M_{Jup} for WD 1620-391.
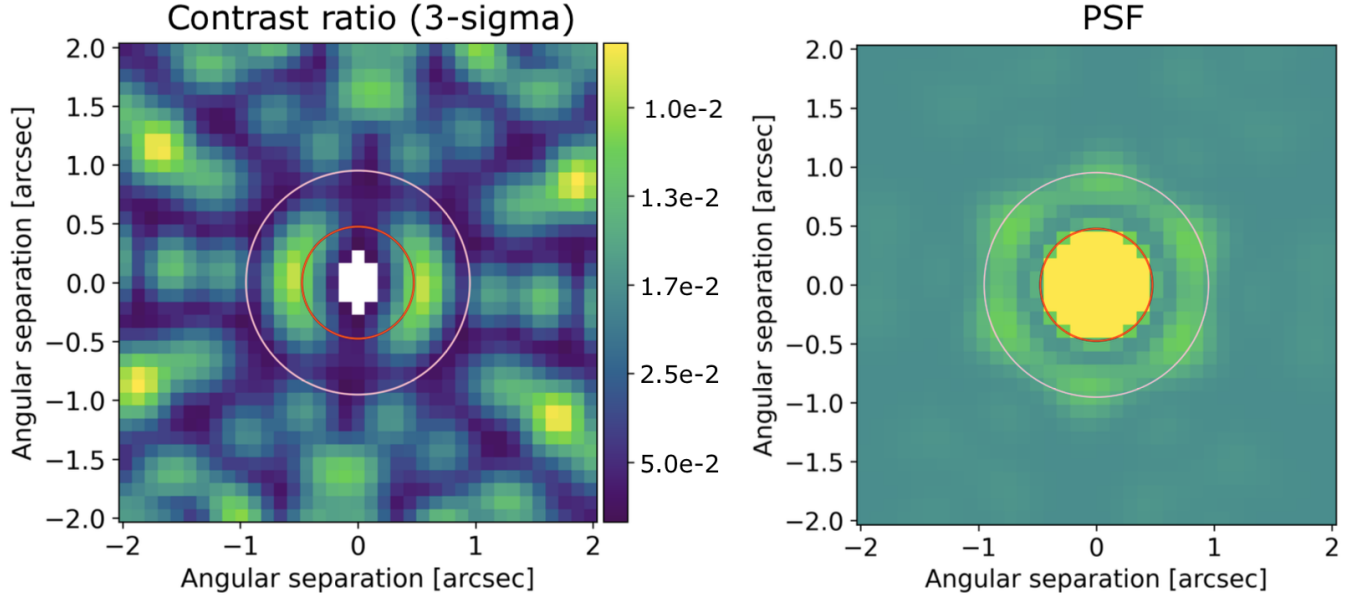
Figure 11. (left) Detection contrast map with KPI for WD2149+021 in the F1500W filter. Light regions correspond to high contrast sensitivity at 3-σ confidence. The red and pink circles represent the $1\,\lambda/D$ and $2\,\lambda/D$ separations. (right) Representative point spread function in the same filter. The best contrasts (in yellow in the left plot, contrast ratio of $\sim$0.01) are achieved at the separation corresponding to the first minimum of the Airy pattern, $\sim 1.22\,\lambda/D$. The other 3 WDs show similar maps, just scaled differently. The contrasts correspond to a 3σ detection in the kernel phase space where binary model kernels are 3 times larger than the standard deviation of the measured kernels.

## 6. INTERPRETATION OF INFRARED EXCESSES AROUND WD 2149+021 AND WD 2105-820

The presence of $\sim$5-σ excesses at F2100W for these two objects implies three likely possibilities: a) low luminosity dust, b) a cool companion radiating thermally, or c) an irradiated companion close to the WD. However, given the fact that we have a singular photometric excess point, it is difficult to find a unique model or answer. We thus work through the existing data to understand what is favored or disfavored for each scenario.

Prior to determining more complex situations, we instead calculate the available physical constraints on the excesses under the assumption of blackbody emission (Farihi et al. 2014; Poulsen et al. 2024). We calculated blackbody emission at a range of temperatures and total emitting areas and determined the hottest and coolest temperatures that succesfully matched the 21 μm excess flux to within 1-σ and did not exceed the 3-σ upper limit excess at 15 μm for WD 2149+021. For WD 2105-820 with a 2-σ excess at 15 μm, we calculated the maximum and minimum temperature/area combinations that matched to within 1-σ of both the 15 and 21 μm excesses for WD 2105-820. WD 2105-820's IR excess is consistent with a blackbody with T_{eff} between 170-280 K and with respective emitting areas between 7×10^{19} cm^2 and 1×10^{19} cm^2 (0.7 and 0.3 R$_{Jup}$). WD 2149+021's excesses are consistent with $T_{eff} < 330$ K and emitting area of $>1.8\times10^{19}$ cm^2 (>0.25 R$_{Jup}$). The implied radii of the excesses are tantalizingly similar to the range of radii seen in the Solar System giant planets and are at least an order of magnitude lower than that seen for typical warm WD debris disks.

6.1. *Cool or Low Luminosity Dust: Possible Disk Structures*

We first consider whether the IR excess could be caused by low luminosity versions of the dust disks seen around other WDs, something hitherto only proposed theoretically before JWST (Bonsor et al. 2017). Typically WDs that show IR excesses between 5-10 μmhave high accretion rates–the typical accretion rates of our targets are about 3 orders of magnitude lower than that seen for a bright disk such as that seen around G29-38 (Xu et al. 2014). In terms of 21 μm luminosity, G29-38 is $\approx$300-500 times brighter than WD 2149+021 and WD 2105-820. Thus, we explore if low luminosity and/or low mass versions of a G29-38 analog disk can match the data such that no excess is seen at wavelengths $<$10 μm, but a significant excess is still present beyond 15 μm.

To test the theory that the observed excess MIR emission is due to a dust disk rather than planet, we generate dust disk models and compare disk emission to the observed excesses. Since spatially resolving a white dwarf dust disk
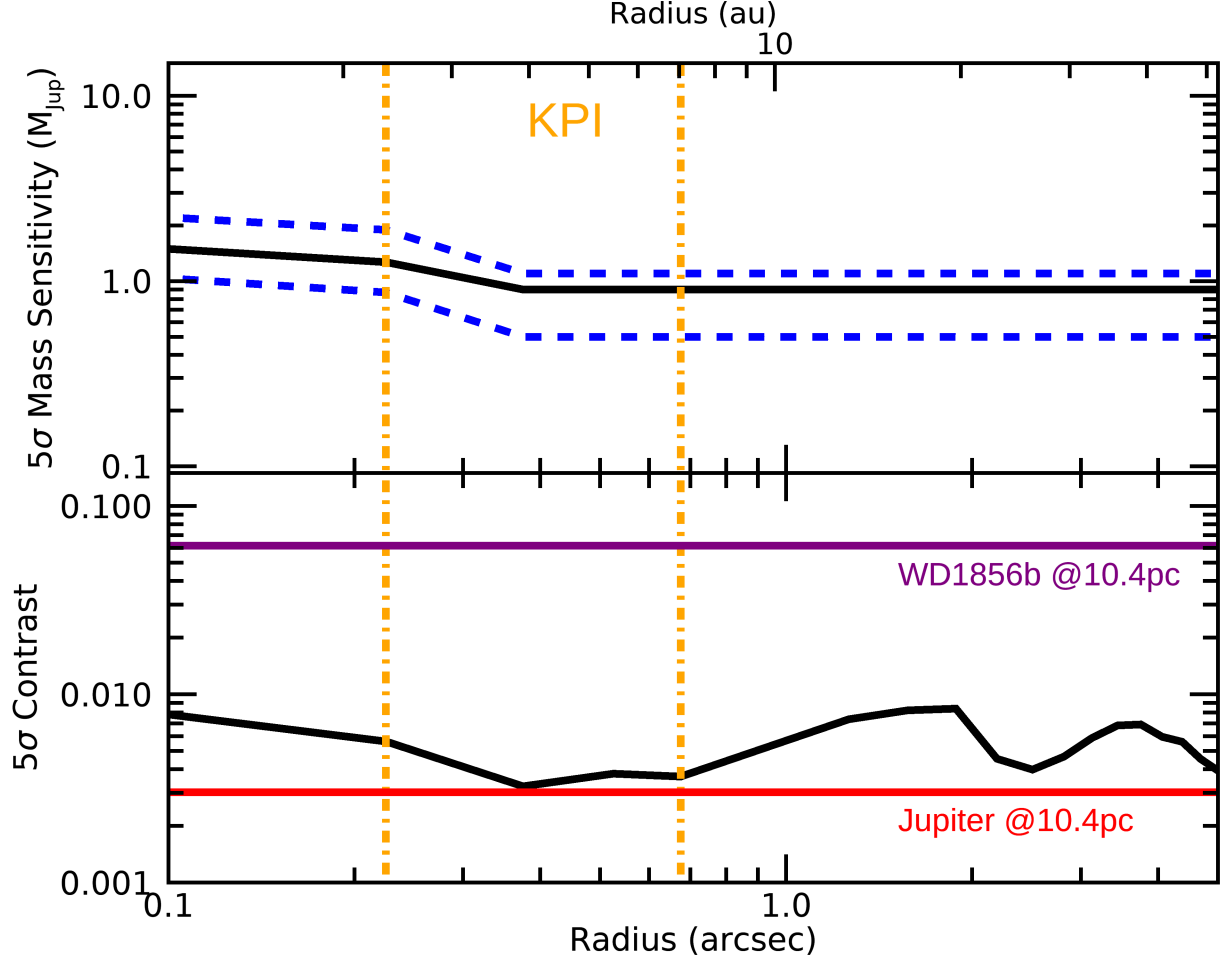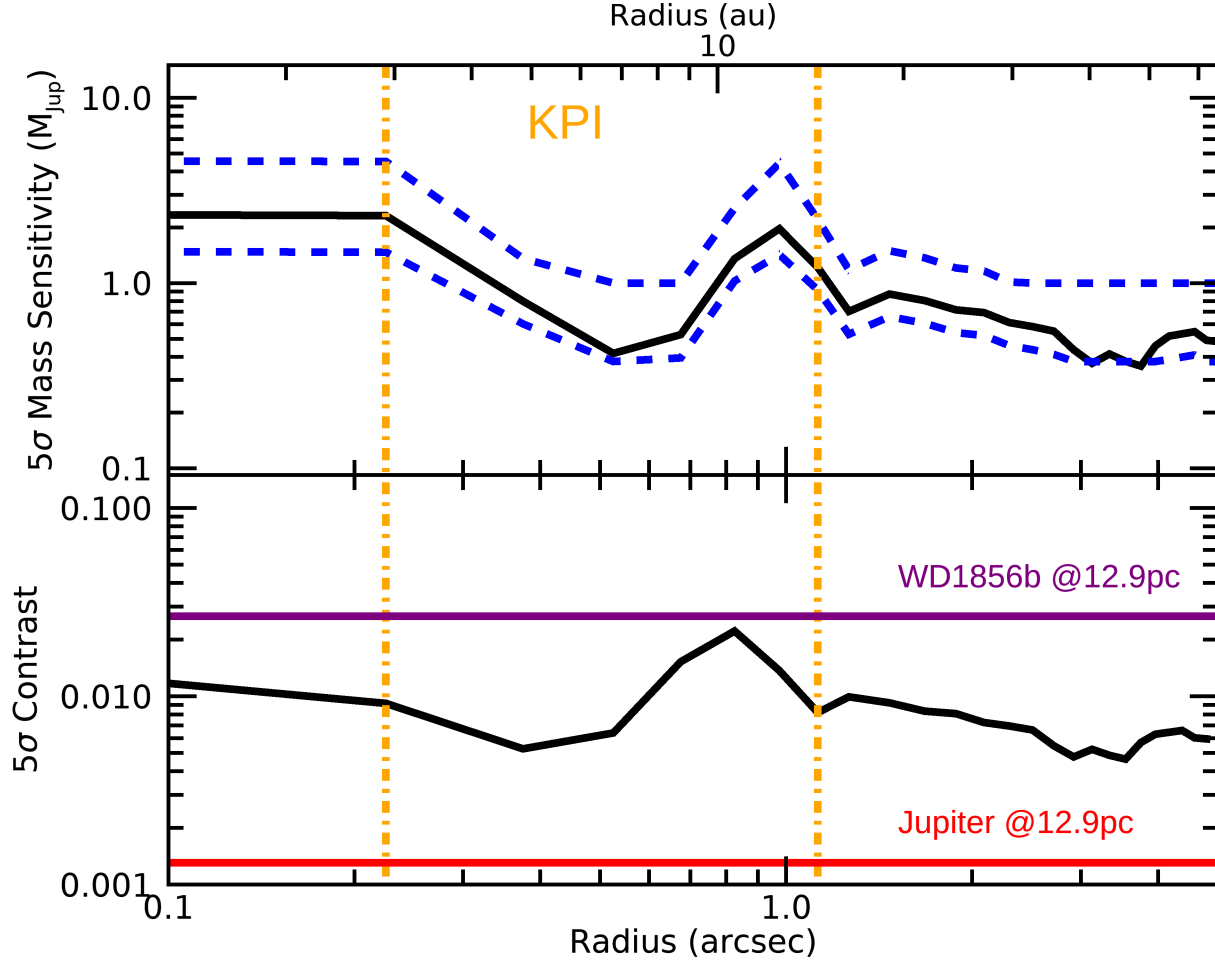
Figure 12. (top) Planet sensitivity curve for WD 1202-232. The black curve represents the 5-σ mass sensitivity limit in F1500W for a combination of KPI analysis ($<0\rlap{.}''5$) and with direct imaging with RDI. The flux ratio contrast is converted into mass sensitivity via the calculated isochrones as described in Section 4. The blue dashed lines show the minimum and maximum masses assuming the age uncertainty of WD 1202-232. The lowest mass allowed by the models is 0.5 $M_{\rm Jup}$, but the contrast sensitivity is a factor of 10 fainter than the predicted flux for 0.5 $M_{\rm Jup}$. (bottom) Contrast sensitivity of the observations represented by the black curve. Overplotted is the expected 15 μm flux ratio of WD1856+584b and Jupiter at 10.4 pc.

is not possible given the size of the disk, the exact structure of a white dwarf dust disk is uncertain, and must be inferred from disk thermal emission. Here, we assume three simple, distinct disk models, differentiated by the inner disk radius, and attempt to describe the observed excesses at WD 2105-820 and WD 2149+021 using each model.

Disk thermal emission models are generated with radiative transfer code MCFOST (Pinte et al. 2006, 2009). Due to a sparsity in data, we are limited to a "by-eye" modeling procedure, where the goodness of fit of a model is determined by if the model describes all photometric detections/upper limits. Significant degeneracy in dust disk parameter combinations producing the same flux at 21 μm leads to wide uncertainties on disk properties. If we however restrict ourselves to a fixed inner radius for each of the three models and vary only the mass of the dust in the disk, we are able to place estimates on how much dust would be required at different radial distances to produce the observed emission. Since we are primarily trying to determine if a dust disk is a plausible explanation for the excesses we observe, an extensive search of parameter space is outside the scope of this paper.

6.1.1. *Warm dust disk near the Roche limit*

To develop a standard white dwarf dust disk model, we reproduce the approach of modeling the bright dust disk orbiting G29-38 presented in Ballering et al. (2022) using MCFOST. Once we generated a disk model that sufficiently
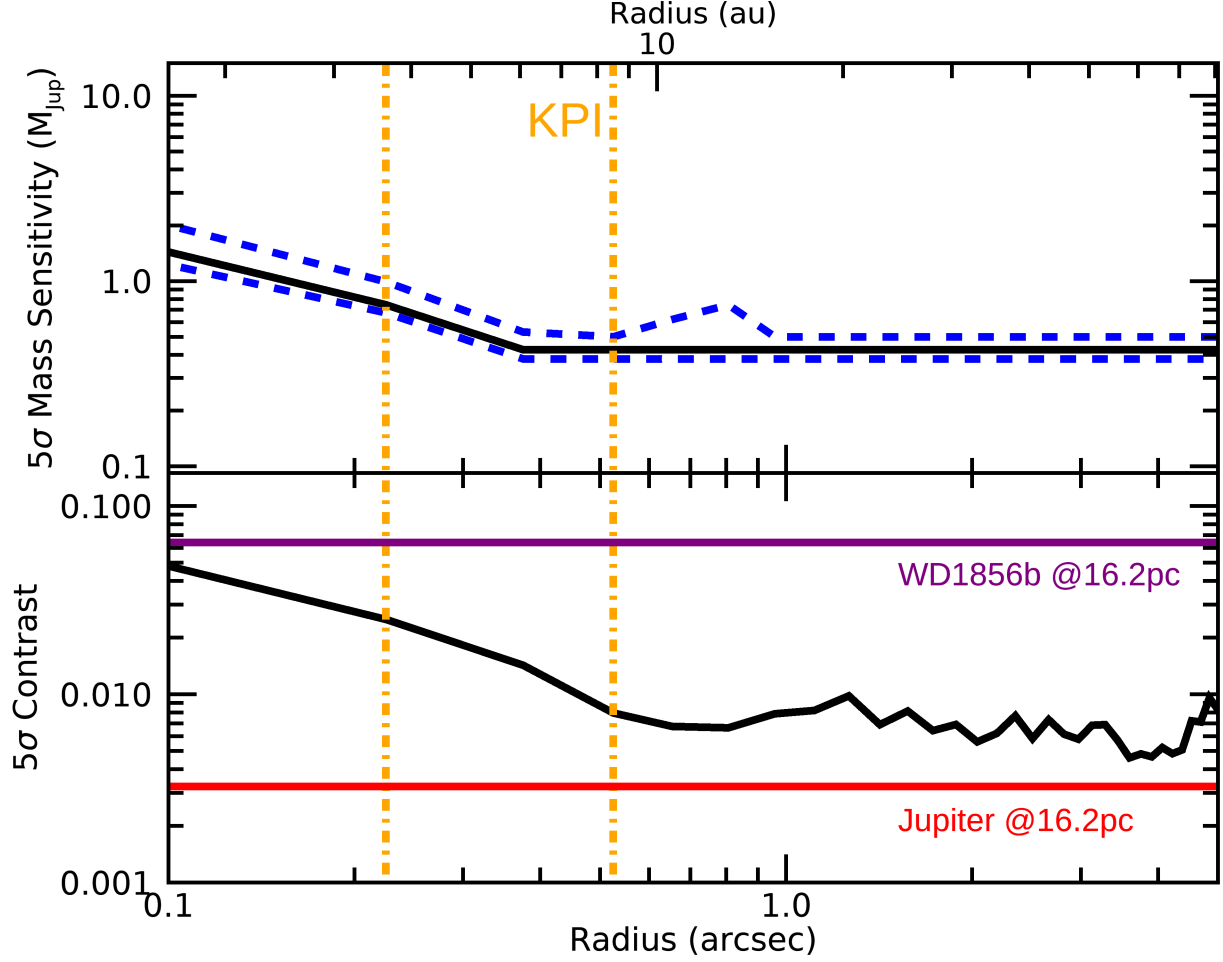
Figure 13. (top) Planet sensitivity curve for WD 1620-391. The black curve represents the 5-σ mass sensitivity limit in F1500W for a combination of KPI analysis ($<0\rlap{.}''5$) and with direct imaging with RDI. The flux ratio contrast is converted into mass sensitivity via the calculated isochrones as described in Section 4. The blue dashed lines show the minimum and maximum masses assuming the age uncertainty of WD 1620-391. The lowest mass allowed by the models is 0.4 $\mathrm{M_{Jup}}$ and the contrast sensitivities are about at that level. (bottom) Contrast sensitivity of the observations represented by the black curve. Overplotted is the expected 15 μm flux ratio of WD1856+584b and Jupiter at 12.9 pc.

fit observations of the G29-38 system, we altered the model to fit the much fainter disks around WD 2105-820 and WD 2149+021.

Disk composition is inferred to be similar to the composition of material accreting onto the photospheres of polluted white dwarfs, which is primarily silicate dominated, bulk Earth material. Reach et al. (2009) finds strong evidence for amorphous carbon, amorphous/crystalline silicates, water ice, and metal sulfides in the material surrounding G29-38 using a detailed modeling approach. When modeling G29-38, Ballering et al. (2022) approximates dust composition using astronomical amorphous silicate optical constants (Draine & Lee 1984), which reproduce the prominent silicate feature. Given that our goal is to determine if a disk is a plausible explanation for the observed excess rather than intricately model disk emission, we use the same constants as Ballering et al. (2022) for consistency between models.

We set the minimum and maximum particle sizes participating in emission at < 4 μm and 10^4 μm, respectively. The distribution of particle sizes is described by a -3.5 power law (Kenyon & Bromley 2017), where smaller particles are more numerous, yet most mass resides in larger dust. Minimum grain size is assumed to be similar to that modeled around G29-38 in Ballering et al. (2022), and maximum grain size is set to be similar to other dusty systems. To
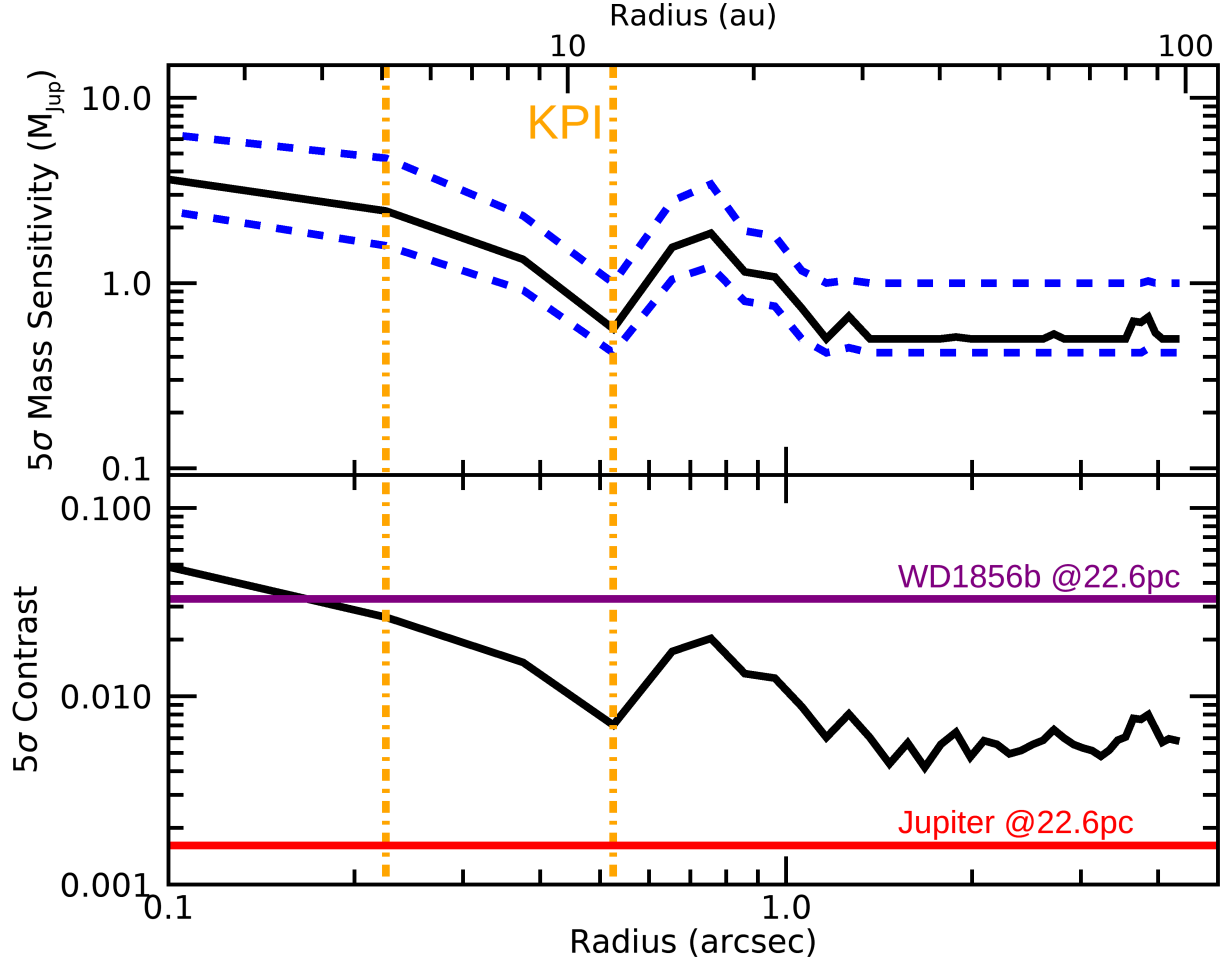
Figure 14. (top) Planet sensitivity curve for WD 2105-820. The black curve represents the 5-σ mass sensitivity limit in F1500W for a combination of KPI analysis ($<0''.5$) and with direct imaging with RDI. The flux ratio contrast is converted into mass sensitivity via the calculated isochrones as described in Section 4. The blue dashed lines show the minimum and maximum masses assuming the age uncertainty of WD 2105-820. The lowest mass allowed by the models is 0.4 $M_{\rm Jup}$, but the contrast sensitivity is a factor of 3 lower than the flux predicted for 0.4 $M_{\rm Jup}$. (bottom) Contrast sensitivity of the observations represented by the black curve. Overplotted is the expected 15 μm flux ratio of WD1856+584b and Jupiter at 16.2 pc.

account for the mass of all particles in the disk, particularly those not participating in emission, we extrapolate the maximum particle size out to 300 km sized bodies for each disk model using the following:

$$M_{disk} = M_{disk}\sqrt{\frac{a_{max,desired}}{a_{max,current}}}$$

White dwarf dust disk location is hypothesized to be set by the sublimation radius and Roche limit of the white dwarf. However, Ballering et al. (2022) finds a more distant disk, with the inner radius existing just exterior to the theoretical Roche limit of the white dwarf (Jura 2003). The likely explanation for the location of the inner radius is that the disk's vertical scale height is larger than the white dwarf's radius, so the bulk of disk emission is from the hot, inner edge of the disk and does not necessarily require significant material closer to the white dwarf. Since the white dwarfs in our sample have masses and radii similar to G29-28, and thus similar Roche radii, we choose inner and outer disk locations close to each white dwarf's Roche radius as was modeled by Ballering et al. (2022). A white dwarf dust disk outer radius of $100-200R_{WD}$ has been observed/modeled in Steele et al. (2021) and directly observed with Doppler tomography in Manser et al. (2016), validating our choice of disk location.

Figure 15. (top) Planet sensitivity curve for WD 2149+021. The black curve represents the 5-σ mass sensitivity limit in F1500W for a combination of KPI analysis ($<0\rlap{.}''5$) and with direct imaging with RDI. The flux ratio contrast is converted into mass sensitivity via the calculated isochrones as described in Section 4. The blue dashed lines show the minimum and maximum masses assuming the age uncertainty of WD 2149+021. The lowest mass allowed by the models is 0.4 $M_{\rm Jup}$, but the contrast sensitivity is 1.5 times fainter than the predicted flux for 0.4 $M_{\rm Jup}$. (bottom) Contrast sensitivity of the observations represented by the black curve. Overplotted is the expected 15 μm flux ratio of WD1856+584b and Jupiter at 22.6 pc.

Dust mass is determined after considering the constraints on other parameters, and we find a narrow range of masses accurately models the data. We fix the gas to dust ratio at 0.1, given that Ballering et al. (2022) did not model gas around G29-38, and we found that the gas to dust ratio did not significantly affect the disk spectrum. We also found no constraint on disk inclination, as our disk models are primarily optically thin and therefore emission does not depend on disk orientation.

6.1.2. *Intermediate disk*

For each target, we additionally produce an intermediate disk model, with an inner radius located around 10 times further from the star than the warm disk model described above. This model was included because a similar dust model can be fit to excesses observed at both 10 and 15 μm in Poulsen et al. 2025 (in prep). For this disk, we assume 10% disk width and a particle size distribution similar to the Ballering et al. (2022) model. However, there is no known scenario that would produce dust in a white dwarf system interior to one AU yet exterior to the white dwarf's Roche limit. Via Jura (2008), material interior to 1 AU with radii smaller than 1-10 km will be removed from the system during stellar evolution, so micron-sized dust in a disk at this location would need to have formed after stellar evolution.
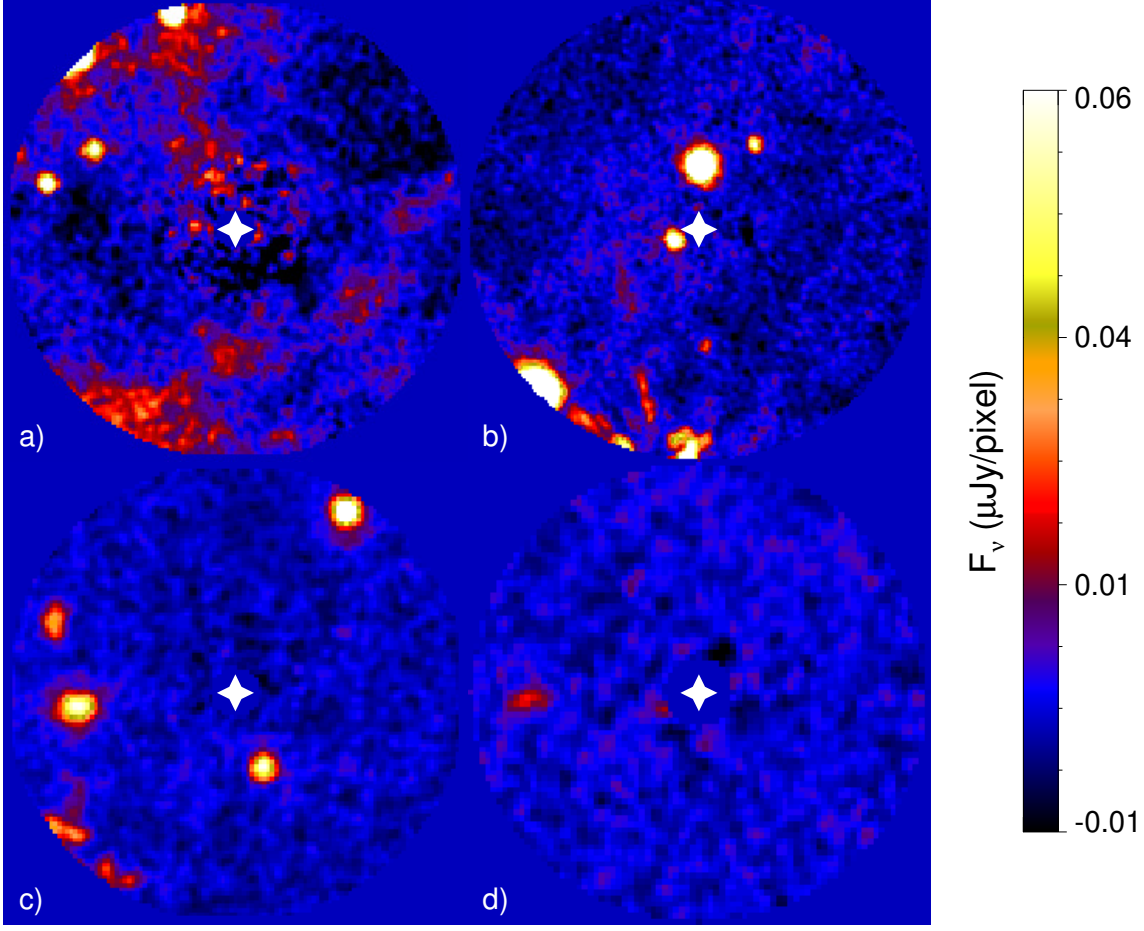
Figure 16. PSF subtracted images of the four WD targets in F1500W. Each panel shows a circular search area of 100 au at the distance of the WD. The orientation of each panel is North up, East left. a) WD 1620-391: Galactic cirrus is present in the background of this image due to its low galactic latitude. Despite this, there are few mid-IR bright objects in the search area. The two point sources to the northeast are consistent with background stars. b) WD 1202-232: three primary sources besides the WD are present. The closest, a point source was reported in Mullally et al. (2024) as a planetary candidate. The others are consistent with background sources: one is spatially resolved and the other is blue across the MIRI filters. c) WD 2105-820: the only point source within a projected separation of 100 au is the planetary candidate to the southwest reported in Mullally et al. (2024). The remaining sources are spatially resolved. d) WD 2149+021: The only significant source within a projected separation of 100 au is a spatially resolved faint galaxy in the background to the East.

6.1.3. *Distant, massive disk*

We also explore the possibility that dust is located in a cold, distant disk between 3 - 3.3 AU, similar to our solar system's asteroid belt. Jura (2008) describes a white dwarf pollution scenario in which the material that forms a dust disk and pollutes the white dwarf photosphere originate in an asteroid belt residual from the progenitor star, altered by the host star's red giant branch evolution. For $1 - 2M_\odot$ progenitor stars such as those in our sample, Jura (2008) predicts asteroids larger than $1 - 10$ km will remain in the disk, while smaller particles will be removed. Such disks would require on the order of 10^{25} g of material, slightly more massive than the solar system disk with a mass of 1.8×10^{24} g.

However, no such disks have been observed around white dwarfs, but this may also be due to a lack of sensitivity to such disks prior to JWST. The only such effort was to detect a solar-system-like asteroid belt around white dwarf G29-38 with a known debris disk (Farihi et al. 2014), which resulted in a non-detection and upper mass limits of 10^{23} g interior to 11 AU. Therefore, we leave this distant disk as a hypothetical, similar to our Solar System's asteroid belt.

6.2. *Comparison of Low Luminosity Disks with 21 μm excesses*
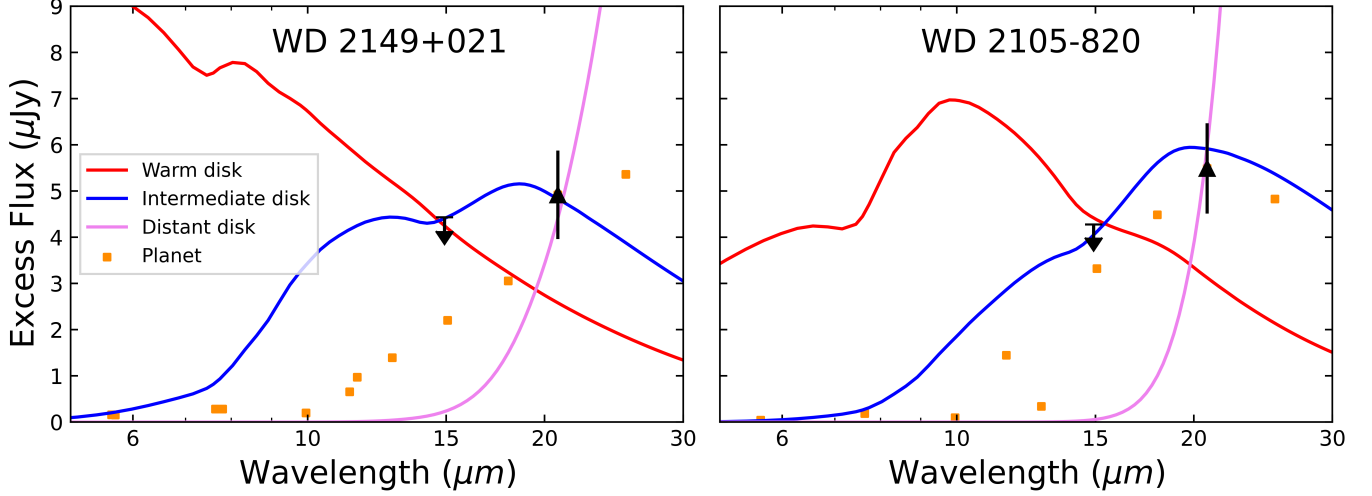
Figure 17. Three different dust disk models fit to observed excess flux at WD 2149+021 and WD 2105-820 after a WD model is subtracted. Black points represent the observed photometric excesses at F2100W, and arrows represent upper detection limits for F1500W for both targets. The planet model fit to WD 2149+021 represents a 202K planet, and the model fit to WD 2105-820 represents a 190K planet.

Disk model	Disk location (AU)	M_{disk} (g)	Particle sizes (μm)
WD 2105-820			
Warm disk at Roche limit	0.0055 - 0.006	1.5×10^{17}	$1.4 - 10^4$
Intermediate disk	0.05-0.055	3.4×10^{18}	$1 - 10^4$
Distant disk	3 - 3.3	2.5×10^{23}	$1 - 10^4$
WD 2149+021			
Warm disk at Roche limit	0.0055 - 0.006	1.5×10^{17}	$1.4 - 10^4$
Intermediate disk	0.05-0.055	2.3×10^{18}	$1 - 10^4$
Distant disk	3 - 3.3	4×10^{21}	$1 - 10^4$

Table 3. Parameters of three different disk models fit to excesses around both white dwarfs in this study.

6.2.1. *WD 2149+021*

WD 2149+021's excess is reasonably described by the distant disk model, and the warm dust disk model is less than 3σ (2.76σ) from the excess at $21\mu m$. An intermediate disk model describes the excess while remaining under the 15 μm detection limit. The distant disk model requires on the order of 10^{21} g of material, which is three orders of magnitude less massive than our solar system's asteroid belt (Binzel et al. 2000). A 203 K planet model accurately describes both the excess and falls below the $15\mu m$ upper limit. Therefore, no disk model can be entirely ruled out.

6.2.2. *WD 2105-820*

The most plausible warm disk model lays at just over 3σ from the $21\mu m$ excess, making it a slightly less likely explanation for the excess. The intermediate disk can be made to describe both constraints. The distant disk model requires on the order of 10^{23} g of mass. However, this represents the mass of particles between $1 - 10^4$ μm, and a distant disk would be expected to contain much larger bodies, which would significantly increase the mass of the disk. N-body simulations of planetary systems perturbing asteroid belts often require more mass than that of the Solar System to explain the high accretion rates seen around other WDs (Debes et al. 2012). A planet model of 190 K can be fit to the 21 μm excesses within 1σ.

6.2.3. *Which Disks are Most Plausible?*

A plausible dust disk with the same structure and similar composition to brighter dusty white dwarf disks, such as that observed around G29-39 (Ballering et al. 2022), can somewhat describe excess MIR emission around both WD

2105-820 and WD 2149+021 if we infer less disk mass. Similarly, a model where a larger mass of dust resides around 3 AU can also be made to fit the excesses, with dust masses between 1 - 10^4 μm grain sizes similar to the mass of the Solar System's asteroid belt. Additionally, the mass of the Eps Eri Belt (Krishnanth et al. 2024) is hypothesized at around 10^{24} g, so we may not rule out the possibility that a further out dust disk causing the excess without more data. While all three kinds of dust disks considered here are somewhat consistent with the data, the intermediate and cold dust disks which best fit the data are not well physically motivated since the RGB and AGB phases of stellar evolution should directly remove most minor bodies from orbital separations <3 au. We thus argue that planetary mass companions are more likely to explain the 21 μm excesses we detect.

Given that reasonable dust disk models can be derived from a faint MIR excess, we demonstrate that JWST has the capabilities to detect and characterize a wider swath of dust disks around white dwarfs than was historically possible with WISE and Spitzer. From disk SED modeling, we predict around >6% disk emission at 10 microns in the scenario of warm dust located close to the star, so a spectrum spanning 5-13 μm taken with the MIRI Low-Resolution Spectrograph (MIRI-LRS) would provide more definitive evidence for the presence of warm dust disks around our targets.

6.3. Thermal Emission from Planets

Similar to dust disks, the presence of an excess at one wavelength can be compared to cool exoplanet atmosphere models to provide a constraint on the possible mass of a planetary companion. This and constraints on how close the planet is to the WD can be used to test models for planetary evolution during post-main sequence evolution. Currently, it is plausible that most Jovian planets survive beyond a given radius (Mustill & Villaver 2012), with a smaller fraction of planets that might be found interior, and virtually no planets interior to this survival radius. Given the small number of targets, it is striking that two WDs show some evidence of a planet being present, with a possibility that WD 2105-820 has both an interior planet and one at 34 au (Mullally et al. 2024).

Based on the distance and 21 μm flux, we compare to the same grid of models used to determine our sensitivity to resolved planetary companions. The excess flux for WD 2149+021, assuming a total system age of 3 Gyr, is consistent with a 3^{+3}_{-2} $M_{\rm Jup}$ companion and a $T_{\rm eff}$=203±16 K. While we quote uncertainties driven by the system age uncertainties, we note that our inferences are heavily dependent on the accuracy of our models, which are largely untested at these temperatures. WD 2105-820's excess is consistent with a $1.4^{+0.4}_{-0.2}$ $M_{\rm Jup}$ companion with $T_{\rm eff}$=171±10 K. If confirmed, these would be the some of the coolest planets yet detected and similar to the recently announced cool planet candidate in orbit around WD 0310-668 ($T_{\rm eff}$=248 K) (Limbach et al. 2024) and the transiting planet orbiting WD 1856+534b ($T_{\rm eff}$=186 K)(Limbach et al. 2025).

A combination of our PSF subtraction and KPI limits for point sources constrains the location of the excesses to be within 4 and 8 au for WD 2105-820 and WD 2149+021 respectively. If we include similar limits from GAIA astrometric noise based on the fact that both stars have renormalized unit weight errors (RUWE) of less than 1.4, the planets would be constrained to reside interior to 2 au (see Limbach et al. 2024).

6.4. Irradiated Planets

As explored in Poulsen et al. (2024) and references therein, close-in exoplanets will also show an IR excess and radiate hotter than would be expected for a given system age. Given the inferred range of temperatures due to these excesses we can also infer the range of orbital radii such planets would reside by estimating an equilibrium temperature based on our blackbody estimates (T_{eq}) (Poulsen et al. 2024):

$$T_{\rm eq} = T_{\rm eff} \left(1 - \alpha\right)^{0.25} \sqrt{\frac{R_{\rm WD}}{2\,a}} \qquad (1)$$

and solving for semi-major axis assuming a geometric albedo α=0.3 and R_{WD}=0.011 $R_{\odot}$ for both WDs. Under these assumptions, our observations are consistent with irradiated planets residing at between 0.02-0.15 au for WD 2149+021 and 0.01-0.1 au for WD 2105-820, corresponding to orbital periods of 1.3-40 d and 0.5-15 d for WD 2149+021 and WD 2105-820, respectively.

7. DISCUSSION

Our study of four white dwarf stars has found intriguing evidence of planetary systems that may be driving the host star's pollution, thus elucidating the type of planetary architecture that most commonly drives the tidal disruption of

Table 4. Summary of candidate planet properties

WD	Unresolved M	Unresolved a_{proj}	Resolved M	Resolved a_{proj}
	(M_{Jup})	(au)	(M_{Jup})	(au)
WD 1202-232	...	...	1	11
WD 2105-820	$1.4^{+0.4}_{-0.2}$	<4	$1.6^{+0.4}_{-0.2}$	34
WD 2149+021	3^{+3}_{-2}	<8	...	...

rocky bodies in orbit around post-main sequence systems. Out of a sample of four polluted white dwarfs, a shocking three targets show evidence of either planets, or dust, or both. We summarize all candidate planets for our systems in Table 4, with new mass estimates for the resolved planet candidates based on a best fit to the 21 μm fluxes and accounting for age uncertainties. We choose the 21 μm flux as the basis for our mass estimate to be consistent with the unresolved excesses. If we include the recent results from the MEOW survey (Limbach et al. 2024), a third metal-polluted white dwarf also shows an infrared excess similar to those seen with our targets, located <2 au from its host. Other planetary mass objects with similar low temperatures to our resolved candidates and unresolved excesses are available for comparison with fluxes observed with JWST: WD 1865+534b (Limbach et al. 2025), a transiting planet at 25 pc with JWST MIRI detections, Eps Indi Bb at 3.6 pc (Matthews et al. 2024), and WD 0806-661b at 19.23 pc (Voyer et al. 2025).

It is interesting to note that one WD in our sample, WD 2105-820, possesses a directly imaged candidate planetary mass companion at ~34 au and the presence of a significant IR excess consistent with a planetary mass companion at closer separation <4 au. Intriguingly, the 21 μm flux of both the IR excess and the companion are equivalent within the uncertainties (Mullally et al. 2024). If both are confirmed to be planets, then this would represent the first multi-planet WD system to be discovered. The inferred masses for both objects then are close to Jupiter's and the difference in separations ~30 au is significantly larger than that seen in our own Solar System. This could hint at the possibility of dynamical interactions that sent one of the giant planets into an eccentric orbit with a large semi-major axis (e.g. Debes & Sigurdsson 2002). If that were true, we would predict that both planets would have eccentric orbits. Gaia DR4 and future JWST MIRI imaging could provide constraints on the orbital parameters of the inner and outer planet respectively.

While it is premature to draw strong conclusions from this study due to small-number statistics, it is helpful to think about possible future trends our work implies, once the IR-excesses we detected are characterized and when the resolved candidates are confirmed or refuted as planetary companions. We thus consider the case where a) all candidates are confirmed as planetary companions, b) only IR-excesses are confirmed as planetary companions, or c) no planetary companions are confirmed and the IR-excesses are due to dust close to the WD.

In the first case, we would be faced with a situation where 75% of our sample stars had at least 1 giant planet with a mass of ~1-5M_{Jup}, at orbital separations that range from as close as a few tenths of an au to 34 au. Despite the small number uncertainties, it would still imply, based on binomial probability statistics for 4 detections in 4 trials, an occurrence rate of giant planets of >55% at 95% confidence. In this scenario giant planets are overrepresented compared to the occurrence rate of giant planets in main sequence star RV surveys (Fernandes et al. 2019) and at a possible range of orbital radii that might directly challenge our notions of planetary survival, particularly if the IR-excess candidates reside at very close orbital separations. This outcome strongly favors the validity of the giant planet driven models of WD accretion (Debes & Sigurdsson 2002, e.g.) and suggest that pollution is not largely driven by widely separated binaries (Veras et al. 2018) or other scenarios that do not require a giant planet (e.g. Zuckerman & Reid 1998; O'Connor et al. 2022).

The second case, where only the infrared excess planets are confirmed, is not that different in result from the first case, with the exception that WD pollution may be driven by a population of giant planets fairly close in primordial orbital separation to Jupiter. With upper limits to orbital separation at 4 and 8 au for WD 2105-820 and WD 2149+021 respectively, the planets may be very close to the minimum survivable distance from the host star when the star was a red giant or asymptotic giant. Mustill & Villaver (2012), using simulations, predicted the final orbital radii of planets

that just escaped engulfment, for both circular and elliptical orbits as a function of initial stellar mass. Assuming the best estimates of initial mass for WD 2105-820 and WD 2149+021 (2.5 and $1.5 M_\odot$, respectively), the outermost surviving planets should reside beyond ∼6 and 3.5 au under the assumption that the initial planet orbits were circular. This puts the WD 2105-820 excess at odds with theoretical predictions which could imply that the planet had a non-circular orbit or that tidal evolution of exoplanets is stronger than predicted.

In the third case where none of the planets are confirmed, if our sample is representative, it would suggest that a large fraction of polluted white dwarfs have cool IR excesses, even at accretion rates that are orders of magnitude smaller than those seen for existing warm WD disks detected at shorter wavelengths. This scenario would then favor a situation where giant planets larger than $1 M_{Jup}$ are not the dominant perturber of minor bodies. It is possible that undetectable lower mass giant planets cause this pollution. Depending on mass, this scenario would most likely require a significant number of lower mass planets to drive the metal pollution (O'Connor et al. 2022).

The results of our exploratory program demonstrate the revolutionary sensitivity that JWST/MIRI has for detecting planetary systems around nearby WDs and represents an opportunity for the future exploration of dead planetary systems, especially for polluted WDs. A search of a larger number of polluted WDs within 25 pc could yield a trove of interesting mid-IR detections and directly imaged planets. One problem is that our knowledge of metal line WDs is incomplete–out of a total of 58 stars within 25 pc and with T_{eff}>9000 K, only 5, or 10%, are known to contain metals, lower than that seen in other samples of warm WDs. This is partially due to new WDs being discovered by *Gaia*, and a lack of high spectral resolution spectra in either the visible or the UV. Ideally, a volume limited search for metals could be conducted to help JWST focus in on the highest value targets.

Moving forward, it is clear that the faintest IR-excesses will be hard to distinguish between plausible debris disks and planetary companions even with JWST. They are sufficiently faint that it is nearly impossible to get a direct spectrum beyond 15 μm and thus will require sensitive searches for silicate emission lines at 10 μm with MIRI/LRS or additional photometry at 18 and 25 μm in the F1800W and F2500W filters with the MIRI imager (e.g. Limbach et al. 2024). Given the lower sensitivity of the F2500W filter, where most cool planet SEDs are peaking and dust SEDs from warmer disks are expected to be getting fainter some of these excesses will have to wait for future observatories sensitive to ∼ μJy sources beyond 25 μm, such as the proposed PRIMA mission.

REFERENCES

Bagnulo, S., & Landstreet, J. D. 2018, A&A, 618, A113, doi: 10.1051/0004-6361/201833235

Ballering, N. P., Levens, C. I., Su, K. Y. L., & Cleeves, L. I. 2022, ApJ, 939, 108, doi: 10.3847/1538-4357/ac9a4a

Bédard, A., Bergeron, P., Brassard, P., & Fontaine, G. 2020, ApJ, 901, 93, doi: 10.3847/1538-4357/abafbe

Bianchi, L., Shiao, B., & Thilker, D. 2017, ApJS, 230, 24, doi: 10.3847/1538-4365/aa7053

Binzel, R., Hanner, M., & Steel, D. 2000, Allen's Astrophysical Quantities, 315, doi: 10.1007/978-1-4612-1186-0_13

Bohlin, R. C., Gordon, K. D., & Tremblay, P. E. 2014, PASP, 126, 711, doi: 10.1086/677655

Bonsor, A., Farihi, J., Wyatt, M. C., & van Lieshout, R. 2017, MNRAS, 468, 154, doi: 10.1093/mnras/stx425

24

Bouchet, P., García-Marín, M., Lagage, P. O., et al. 2015, PASP, 127, 612, doi: 10.1086/682254

Burleigh, M. R., Clarke, F. J., & Hodgkin, S. T. 2002, MNRAS, 331, L41, doi: 10.1046/j.1365-8711.2002.05417.x

Debes, J., Sankrit, R., Fischer, T., et al. 2024, The Hubble Advanced Spectral Product (HASP) Program, Instrument Science Report COS 2024-01, 31 pages

Debes, J. H., & Sigurdsson, S. 2002, ApJ, 572, 556, doi: 10.1086/340291

Debes, J. H., Sigurdsson, S., & Hansen, B. 2007, AJ, 134, 1662, doi: 10.1086/521394

Debes, J. H., Sigurdsson, S., & Woodgate, B. E. 2005, AJ, 130, 1221, doi: 10.1086/432660

Debes, J. H., Walsh, K. J., & Stark, C. 2012, ApJ, 747, 148, doi: 10.1088/0004-637X/747/2/148

Dicken, D., Marín, M. G., Shivaei, I., et al. 2024, A&A, 689, A5, doi: 10.1051/0004-6361/202449451

Draine, B. T., & Lee, H. M. 1984, ApJ, 285, 89, doi: 10.1086/162480

Dupuis, J., Fontaine, G., Pelletier, C., & Wesemael, F. 1992, ApJS, 82, 505, doi: 10.1086/191728

Eggen, O. J., & Greenstein, J. L. 1965, ApJ, 141, 83, doi: 10.1086/148091

Farihi, J., Wyatt, M. C., Greaves, J. S., et al. 2014, MNRAS, 444, 1821, doi: 10.1093/mnras/stu1545

Fernandes, R. B., Mulders, G. D., Pascucci, I., Mordasini, C., & Emsenhuber, A. 2019, ApJ, 874, 81, doi: 10.3847/1538-4357/ab0300

Gentile Fusillo, N. P., Tremblay, P. E., Jordan, S., et al. 2018, MNRAS, 473, 3693, doi: 10.1093/mnras/stx2584

Gordon, K. D., Bohlin, R., Sloan, G. C., et al. 2022, AJ, 163, 267, doi: 10.3847/1538-3881/ac66dc

Gordon, K. D., Sloan, G. C., Garcia Marin, M., et al. 2025, AJ, 169, 6, doi: 10.3847/1538-3881/ad8cd4

Hogan, E., Burleigh, M. R., & Clarke, F. J. 2009, MNRAS, 396, 2074, doi: 10.1111/j.1365-2966.2009.14565.x

Holberg, J. B., & Bergeron, P. 2006, AJ, 132, 1221, doi: 10.1086/505938

Holberg, J. B., Bruhweiler, F. C., & Andersen, J. 1995, ApJ, 443, 753, doi: 10.1086/175565

Jordan, S., Aznar Cuadrado, R., Napiwotzki, R., Schmid, H. M., & Solanki, S. K. 2007, A&A, 462, 1097, doi: 10.1051/0004-6361:20066163

Jura, M. 2003, ApJL, 584, L91, doi: 10.1086/374036

—. 2008, AJ, 135, 1785, doi: 10.1088/0004-6256/135/5/1785

Kammerer, J., Ireland, M. J., Martinache, F., & Girard, J. H. 2019, MNRAS, 486, 639, doi: 10.1093/mnras/stz882

Kammerer, J., Cooper, R. A., Vandal, T., et al. 2023, PASP, 135, 014502, doi: 10.1088/1538-3873/ac9a74

Kawka, A., Vennes, S., Schmidt, G. D., Wickramasinghe, D. T., & Koch, R. 2007, ApJ, 654, 499, doi: 10.1086/509072

Kenyon, S. J., & Bromley, B. C. 2017, ApJ, 850, 50, doi: 10.3847/1538-4357/aa9570

Kilkenny, D., O'Donoghue, D., Koen, C., Stobie, R. S., & Chen, A. 1997, MNRAS, 287, 867, doi: 10.1093/mnras/287.4.867

Koester, D., Gänsicke, B. T., & Farihi, J. 2014, A&A, 566, A34, doi: 10.1051/0004-6361/201423691

Koester, D., Rollenhagen, K., Napiwotzki, R., et al. 2005, A&A, 432, 1025, doi: 10.1051/0004-6361:20041927

Krishnanth, P. M. S., Douglas, E. S., Anche, R. M., et al. 2024, AJ, 168, 169, doi: 10.3847/1538-3881/ad6efe

Landstreet, J. D., Bagnulo, S., Valyavin, G. G., et al. 2012, A&A, 545, A30, doi: 10.1051/0004-6361/201219829

Limbach, M. A., Vanderburg, A., Stevenson, K. B., et al. 2022, MNRAS, 517, 2622, doi: 10.1093/mnras/stac2823

Limbach, M. A., Vanderburg, A., Venner, A., et al. 2024, ApJL, 973, L11, doi: 10.3847/2041-8213/ad74ed

Limbach, M. A., Vanderburg, A., MacDonald, R. J., et al. 2025, ApJL, 984, L28, doi: 10.3847/2041-8213/adc9ad

Linder, E. F., Mordasini, C., Mollière, P., et al. 2019, A&A, 623, A85, doi: 10.1051/0004-6361/201833873

Luyten, W. J. 1949, ApJ, 109, 528, doi: 10.1086/145156

Malamut, C., Redfield, S., Linsky, J. L., Wood, B. E., & Ayres, T. R. 2014, ApJ, 787, 75, doi: 10.1088/0004-637X/787/1/75

Manser, C. J., Gänsicke, B. T., Marsh, T. R., et al. 2016, MNRAS, 455, 4467, doi: 10.1093/mnras/stv2603

Marley, M., Saumon, D., Morley, C., et al. 2021, Sonora Bobcat: cloud-free, substellar atmosphere models, spectra, photometry, evolution, and chemistry [Data set], Sonora Bobcat, Zenodo, doi: 10.5281/zenodo.5063476

Marsh, M. C., Barstow, M. A., Buckley, D. A., et al. 1997, MNRAS, 287, 705, doi: 10.1093/mnras/287.4.705

Martinache, F. 2010, ApJ, 724, 464, doi: 10.1088/0004-637X/724/1/464

Matthews, E. C., Carter, A. L., Pathak, P., et al. 2024, Nature, 633, 789, doi: 10.1038/s41586-024-07837-8

Mayor, M., Udry, S., Naef, D., et al. 2004, A&A, 415, 391, doi: 10.1051/0004-6361:20034250

Mullally, S. E., Mullally, F., Albert, L., et al. 2021, A Search for the Giant Planets that Drive White Dwarf Accretion, JWST Proposal. Cycle 1, ID. #1911

Mullally, S. E., Debes, J., Cracraft, M., et al. 2024, ApJL, 962, L32, doi: 10.3847/2041-8213/ad2348

Mustill, A. J., & Villaver, E. 2012, ApJ, 761, 121, doi: 10.1088/0004-637X/761/2/121

Napiwotzki, R., Karl, C. A., Lisker, T., et al. 2020, A&A, 638, A131, doi: 10.1051/0004-6361/201629648

O'Connor, C. E., Teyssandier, J., & Lai, D. 2022, MNRAS, 513, 4178, doi: 10.1093/mnras/stac1189

Pinte, C., Harries, T. J., Min, M., et al. 2009, A&A, 498, 967, doi: 10.1051/0004-6361/200811555

Pinte, C., Ménard, F., Duchêne, G., & Bastien, P. 2006, A&A, 459, 797, doi: 10.1051/0004-6361:20053275

Pope, B., Martinache, F., & Tuthill, P. 2013, ApJ, 767, 110, doi: 10.1088/0004-637X/767/2/110

Poulsen, S., Debes, J., Cracraft, M., et al. 2024, AJ, 167, 257, doi: 10.3847/1538-3881/ad374c

Reach, W. T., Lisse, C., von Hippel, T., & Mullally, F. 2009, ApJ, 693, 697, doi: 10.1088/0004-637X/693/1/697

Rodrigo, C., Cruz, P., Aguilar, J. F., et al. 2024, A&A, 689, A93, doi: 10.1051/0004-6361/202449998

Steele, A., Debes, J., Xu, S., Yeh, S., & Dufour, P. 2021, ApJ, 911, 25, doi: 10.3847/1538-4357/abc262

Stephenson, C. B., Sanduleak, N., & Hoffleit, D. 1968, PASP, 80, 92, doi: 10.1086/128591

van Maanen, A. 1919, PASP, 31, 42, doi: 10.1086/122810

Veras, D., Xu, S., & Rebassa-Mansergas, A. 2018, MNRAS, 473, 2871, doi: 10.1093/mnras/stx2141

Voyer, M., Changeat, Q., Lagage, P.-O., et al. 2025, ApJL, 982, L38, doi: 10.3847/2041-8213/adbd46

Wegner, G. 1978, MNRAS, 182, 111, doi: 10.1093/mnras/182.2.111

Wolff, B., Kruk, J. W., Koester, D., et al. 2001, A&A, 373, 674, doi: 10.1051/0004-6361:20010612

Xu, S., Jura, M., Koester, D., Klein, B., & Zuckerman, B. 2014, ApJ, 783, 79, doi: 10.1088/0004-637X/783/2/79

Zuckerman, B., Koester, D., Reid, I. N., & Hünsch, M. 2003, ApJ, 596, 477, doi: 10.1086/377492

Zuckerman, B., & Reid, I. N. 1998, ApJL, 505, L143, doi: 10.1086/311608